JOURNAL OF PETROLOGY

Journal of Petrology, 2018, Vol. 59, No. 4, 589–612
doi: 10.1093/petrology/egy038
Advance Access Publication Date: 14 April 2018
Original Article

OXFORD

Bulk and Mush Melt Evolution in Agpaitic Intrusions: Insights from Compositional Zoning in Eudialyte, Ilímaussaq Complex, South Greenland

Anouk M. Borst[1,2]*, Henrik Friis[3], Troels F. D. Nielsen[1] and Tod E. Waight[2]

[1]Department of Petrology and Economic Geology, Geological Survey of Denmark and Greenland, Øster Voldgade 10, 1350 Copenhagen, Denmark; [2]Department of Geosciences and Natural Resource Management (Geology Section), University of Copenhagen, Øster Voldgade 10, 1350 Copenhagen, Denmark; [3]Natural History Museum, University of Oslo, P.O. 1172, Blindern, 0318 Oslo, Norway

*Corresponding author. Present address: School of Geography and Geosciences, University of St Andrews, North Street, KY16 9AL St Andrews, Fife, UK. Tel: +447874914096. E-mail: amb43@st-andrews.ac.uk

ABSTRACT

The kakortokites of the Mesoproterozoic Ilímaussaq complex, South Greenland, comprise a rhythmically layered series of agpaitic nepheline syenites that crystallized at the base of a shallow crustal magma chamber. They host eudialyte-group minerals (EGM), i.e. structurally complex Na-zirconosilicates, as a major cumulate phase, and have attracted considerable interest as a potential resource for rare earth elements (REE), Zr, Nb, Hf and Ta. The origin of the macrorhythmic (c. 8 m) layering has been the subject of much debate, and both open system processes including nucleation cycles induced by periodic replenishment of the magma chamber, and closed system mechanisms involving gravitational sorting and crystal mat formation, have recently been hypothesized. Here we present new compositional data on eudialyte cores and overgrowths from the full layered series and part of the overlying lujavrites to reflect on the proposed models for the kakortokite layering and overall evolution of the complex. Based on these data we argue for continuous bulk liquid fractionation and *in situ* fractionation in macrorhythmic compartments of kakortokite mush gradually building up from the floor of the magma chamber. Eudialyte in the kakortokites displays complex magmatic zoning patterns, typically comprising a sector- and oscillatory-zoned core with subhedral concentric overgrowths. Sector-zoned eudialyte cores reveal stratigraphical fractionation trends of decreasing Ca/(REE + Y), Fe/Mn, Ti, Nb and Cl contents upwards through the layered series. These are interpreted to reflect continuous differentiation of a single agpaitic bulk melt and support models for closed system evolution of the kakortokites. Upward trends become more pronounced in the overlying lujavrites (decreasing Ca/(REE + Y), Fe/Mn, Zr/Hf and Cl), while others remain constant (Ti), or are even reversed (Nb). Eudialyte overgrowths have compositions that diverge from the overall fractionation trends recorded in the cores, and also vary systematically across the sequence. These overgrowths are interpreted to reflect *in situ* fractionation trends of intercumulus mush melts that were chemically isolated from the bulk magma following compartmentalization of the crystal mush. As such, EGM overgrowths are interpreted to record changing layering dynamics as well as varying co-crystallizing intercumulus phase assemblages at the kakortokite–lujavrite transition. The data provide new insights into the geochemical evolution of the Ilímaussaq complex, with broader implications on the emplacement and layering mechanisms operating in peralkaline systems, and demonstrate the importance of detailed petrographic and *in situ* mineral chemical analyses where zoned minerals record contrasting evolution of bulk and mush melts. Deciphering such records is fundamental to understanding the full complexity of magma chamber processes.

Key words: eudialyte; Ilímaussaq; layered intrusions; magma chambers; peralkaline nepheline syenites

INTRODUCTION

Layered intrusions preserve detailed records of magmatic and post-magmatic processes in crustal magma chambers (e.g. Wager & Brown, 1967; Parsons, 1987; Cawthorn, 1996). They are of wide scientific and commercial interest because of their often perplexing magmatic layering and differentiation trends, and their common association with economic deposits of for example Cr, V and platinum-group elements (in mafic systems; Cawthorn *et al.*, 2005; Nielsen *et al.*, 2015), and high field strength elements (HFSE; i.e. Zr, Nb, Hf, Ta and rare earth elements (REE)), U, Th, Zn, Be and Li (in alkaline systems; Sørensen, 1992; Chakhmouradian & Zaitsev, 2012). Many theories on igneous differentiation, layering and cumulate processes derive from studies of mafic–ultramafic intrusions such as Skaergaard and Bushveld (e.g. Wager *et al.*, 1960; Wager & Brown, 1967; McBirney & Noyes, 1979; Charlier *et al.*, 2015, Nielsen *et al.*, 2015). How such processes operate in chemically more complex (peralkaline) systems is less well constrained, partly because quantitative petrogenetic modelling of such systems is hindered by limited thermodynamic data and poorly characterized partition coefficients, phase relations, and melt compositions. A well-studied example is the Mesoproterozoic Ilímaussaq complex in South Greenland, renowned for its exceptional three-dimensional exposure, unique rock types, igneous layering and multi-element resource potential (e.g. Sørensen, 1997, 2001; Bailey *et al.*, 2001; Markl *et al.*, 2001, 2010; Marks *et al.*, 2004, 2011; Sørensen *et al.*, 2006*a*, 2011; Bons *et al.*, 2014; Andersen & Friis, 2015; Marks & Markl, 2015, 2017).

The Ilímaussaq complex is the type locality for agpaitic suites of peralkaline nepheline syenites, i.e. those containing complex Na–Zr–Ti-silicates, such as eudialyte-group minerals (EGM) and rinkite, as the main hosts for HFSE (e.g. Ussing, 1912; Sørensen, 1997; Marks & Markl, 2017). The lowermost exposed part of the complex comprises a series of 29 repetitive, modally layered agpaitic nepheline syenite units, known as kakortokites (Bohse *et al.*, 1971). Each unit ideally comprises a black, a red, and a thicker white sublayer, respectively enriched in the major minerals arfvedsonite, EGM and alkali feldspar plus nepheline. Although the kakortokites represent one of the world's finest examples of macrorhythmic igneous layering, how they formed remains highly debated. Proposed mechanisms include one or a combination of the following: (i) intermittent crystallization of amphibole, EGM and feldspar by fluctuations in intensive parameters, e.g. temperature or vapor pressure in the bulk liquid (e.g. Ussing, 1912; Sørensen, 1969; Sørensen and Larsen, 1987; Pfaff *et al.*, 2008; Hunt *et al.*, 2017); (ii) repeated magma recharge (e.g. Pfaff *et al.*, 2008; Hunt *et al.*, 2017); (iii) crystallization of a compositionally stratified magma chamber (Larsen & Sørensen, 1987); (iv) episodic convective overturns (Bohse *et al.*, 1971); and (v) crystal mat formation by density segregation (Bons *et al.*, 2014; Lindhuber *et al.*, 2015). Most models invoke density segregation of liquidus phases to explain the internal modal layering of individual macrorhythmic units; this is particularly important in the mat formation model (Bons *et al.*, 2014). The importance of gravitational settling in producing the layers was recently disputed by Hunt *et al.* (2017) based on textural studies of macrorhythmic layer unit 0. They suggested that amphibole and EGM successively crystallized *in situ* at the base of the unit as a result of a replenishment-nucleation event, and extrapolated this as a possible layering mechanism for the entire sequence.

Compositional trends in EGM have been used as primary lines of evidence in all of the proposed layering and magma chamber evolution models. Eudialyte-group minerals are ideal monitors for magmatic evolution because of their wide compositional variability and sensitivity to changes in melt or fluid compositions, volatile activities and redox conditions (e.g. Schilling *et al.*, 2011). Previous work on kakortokite EGM compositions, however, revealed surprisingly limited upward fractionation trends (Pfaff *et al.*, 2008), in which the EGM generally approach eudialyte *sensu stricto* compositions (Table 1). More significant variations were recorded in EGM Fe/Mn ratios within individual kakortokite units, i.e. gradually decreasing from the black base to the white top and shifting back to higher values at the base of the overlying black unit (Bons *et al.*, 2014; Lindhuber *et al.*, 2015). These crypto-rhythmic trends formed the basis for the mat formation model, but were alternatively explained by the influx of more primitive Fe-rich melts at the base of each tripartite unit (Hunt *et al.*, 2017).

More controversy exists concerning the intrusive relationship between the kakortokites and the overlying lujavrites (melanocratic nepheline syenites), where EGM record more pronounced upward changes towards Mn-, REE- and Nb-rich and Cl-poor varieties (kentbrooksite component, Table 1; Pfaff *et al.*, 2008; Ratschbacher *et al.*, 2015). A recurring problem in the discussion of the layering and evolution of the kakortokite–lujavrite sequence is the lack of recorded mineral compositional trends across the lower layered series. To address this issue, we present major, minor and trace element data for EGM from the full kakortokite sequence and part of the overlying lujavrites. Crystal-scale, unit-scale and overall stratigraphic compositional trends in EGM are now identified, and upward fractionation trends recognized in both cores and overgrowths. The data provide new constraints on bulk liquid and mush melt evolution

Table 1: List of minerals mentioned in the text

Mineral	Abbreviation	Chemical Formula	Reference
Aluminosilicates			
Alkali feldspar	Afs	$(Na, K)AlSi_3O_8$	1
Analcime	Anl	$NaAlSi_2O_6{\cdot}H_2O$	1
Natrolite	Nat	$Na_2AlSi_3O_{10}{\cdot}2H_2O$	1
Naujakasite	Naj	$Na_6Fe^{2+}Al_4Si_8O_{26}$	
Nepheline	Ne	$(Na, K)AlSiO_4$	1
Sodalite	Sod	$Na_4Al_3Si_3O_{12}Cl$	1
Fe–Ti silicates			
Aegirine	Aeg	$NaFe^{3+}Si_2O_6$	1
Aenigmatite	Aen	$Na_2Fe^{2+}_5TiSi_6O_{20}$	1
Arfvedsonite	Arf	$Na_3Fe^{2+}_4Fe^{3+}Si_8O_{22}(OH)_2$	1
REE minerals			
A1	A1	$HCa_3REE_6(SiO4)_6(F,\square)$	2
Britholite-(Ce)	Brt	$(Ca, Ce)_5(SiO_4, PO_4)_3(OH, F)$	1
Monazite-(Ce)	Mnz	$(Ce, La, Nd, Th)PO_4$	1
Steenstrupine-(Ce)	Ste	$Na_{14}Ce_6Mn_2Fe_2(Zr, Th)(PO_4)_7(Si_6O_{18})_2(OH)_2{\cdot}3H_2O$	3
Na–Zr-silicates			
Catapleiite	Cat	$(Na, Ca)_2ZrSi_3O_9{\cdot}2H_2O$	1
EGM general formula	EGM	$Na_{15}M1_3M2_6Zr_3M3Si_{25}O_{72}\,(O, OH, H_2O)_3X_2$	1
Eudialyte s.l*		$(Na, K, Sr)_{15}(Ca, REE)_6(Fe, Mn)_3(Zr, Ti, Hf)_3(Si, Nb)(Si, Al)Si_{24}O_{72}(O, OH, H_2O)_3(Cl, OH)_2$	4, 5
Eudialyte s.s.**		$Na_{15}Ca_6Fe_3Zr_3SiSi_{25}O_{72}(O, OH, H_2O)_3(Cl, OH)_2$	5
Kentbrooksite**		$Na_{15}Ca_6Mn_3Zr_3NbSi_{25}O_{72}(O, OH, H_2O)_3(F, OH)_2$	5
Gittinsite	Git	$CaZrSi_20_7$	1
Zircon	Zrc	$ZrSiO_4$	1
Ti–Nb–F disilicates			
Nacareniobsite-(Ce)	Ncr	$Na_3Ca_3REENb(Si_2O_7)_2OF_3$	1
Rinkite	Rnk	$Na_2Ca_4REE(Ti, Nb)(Si_2O_7)_2(O, F)_4$	1
Accessories			
Galena	Gl	PbS	1
Thorite	Tho	$(Th, U)SiO_4$	1

*Typical site occupations for the Ilímaussaq EGM suite.
**Dominant endmembers in Ilímaussaq EGM solid solution series.
1: International Mineralogical Association (2016), 2: Karup-Møller & Rose-Hansen (2013), 3: Khomyakov & Sørensen (2001), 4: Pfaff *et al.* (2008), 5: Johnsen & Grice (1999).

and allow for a re-juvenated discussion on the formation of the kakortokite–lujavrite sequence.

GEOLOGY

The Ilímaussaq complex (1160 ± 5 Ma; Krumrei *et al.*, 2006) is an oval-shaped composite intrusion, part of the rift-related Mesoproterozoic Gardar province of South Greenland. The Gardar province comprises a suite of dyke swarms, central intrusive complexes and a volcanic–sedimentary graben fill sequence (Eriksfjord formation), all emplaced in and onto a Paleoproterozoic (Ketilidian, *c.* 1·8 Ga; Garde *et al.*, 2002) and Archaean basement during two discrete episodes of continental rifting between 1·35 and 1·14 Ga (Upton *et al.*, 2003; Upton, 2013). The Ilímaussaq complex is part of the younger Gardar rift and was emplaced at *c.* 3 to 4 km depth (Krumrei *et al.*, 2007), at the erosive contact between Ketilidian granites (Julianehåb batholith) and basalts and sandstones of the Eriksfjord formation (Fig. 1).

The Ilímaussaq complex extends *c.* 17 by 8 km, with roughly 1500 m of vertical exposure. Emplacement occurred by at least four melt batches of peralkaline to alkaline melt derived from a common deep-seated magma chamber (Larsen & Sørensen, 1987; Sørensen *et al.*, 2006*a*). The first batch crystallized Si-oversaturated to weakly undersaturated augite syenites and the second a thin sheet of Si-saturated peralkaline granites and quartz syenites, preserved in the roof of the complex. This was followed by volumetrically dominant agpaitic nepheline syenites. The latter are structurally divided into a roof and a floor sequence, separated by a sandwich horizon containing the most evolved melts. Pulaskite, foyaite, sodalite foyaite and naujaite crystallized sequentially from the top down to form the roof sequence (batch 3). The naujaite is volumetrically dominant and represents a c. 600 m thick poikilitic flotation cumulate of hexagonal and dodecahedral sodalite crystals (up to 75%) enclosed by large (>10 cm) oikocrystic alkali feldspar, nepheline, EGM, aegirine and arfvedsonite. The naujaite displays macro-layering defined by decimetre scale pegmatite horizons, inferred to have formed through volatiles accumulating under the roof (e.g. Ferguson, 1964; Andersen *et al.*, 1981). The floor sequence, focused on here, comprises a macrorhythmic sequence of medium to coarse grained kakortokites (Bohse *et al.*, 1971). These are overlain by mineralogically similar but finer-grained melanocratic nepheline syenites (lujavrites), which together with the kakortokites form batch 4 (Sørensen *et al.*, 2006*a*) and occur in aegirine and arfvedsonite dominated varieties (see detailed descriptions in Ratschbacher *et al.*, 2015). The lujavrite intrudes both roof and country rocks

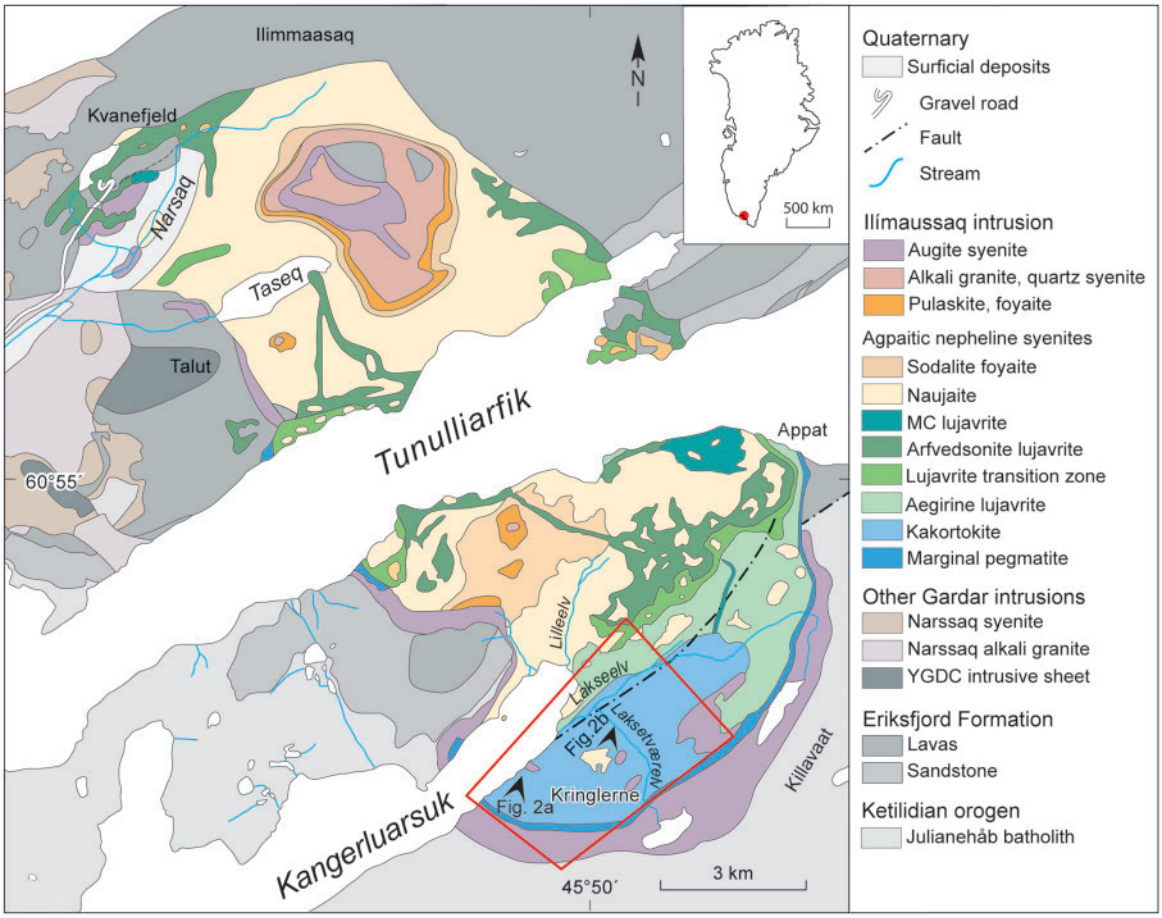

Fig. 1. Geological map of the Ilímaussaq complex, modified after Upton (2013). Red box indicates the study area. Black arrows mark locations of Figures 2 and 3. Abbreviations in legend: YGDC, Younger Giant Dyke Complex; MC, medium- to coarse-grained.

(e.g. Bailey *et al.*, 2006; Sørensen *et al.*, 2006*a*, 2011; Ratschbacher *et al.*, 2015) and envelopes numerous meter-sized autoliths detached from the roof and walls (Figs 2 and 3).

Kakortokite and lujavrite subdivisions

The kakortokites are only exposed in the southern half of the complex and are divided into three sub-units; the lower layered kakortokites (LLK), the slightly layered kakortokites (SLK) and the transitionally layered kakortokites (TLK; Fig. 3; Bohse *et al.*, 1971; Bohse & Andersen, 1981). The LLK represent the 'classic' rhythmically layered kakortokites with a total thickness of *c.* 210 m, which at depth are in contact with finer grained syenitic rocks of tephri-phonolitic composition (Schønwandt *et al.*, 2016). Twenty-nine rhythmic units have been mapped (Bohse *et al.*, 1971), each comprising a basal black layer rich in arfvedsonite, a thin (sometimes poorly developed) red layer rich in EGM and an upper white layer enriched in alkali feldspar and nepheline (Fig. 2). The exposed tripartite units are numbered from -11 to +17, relative to a well-developed marker horizon, unit 0. Individual black, red or white layers within the units are suffixed B, R or W, referring to their respective colours (Bohse *et al.*, 1971). All units are unique in terms of texture, lamination features, mineral grading, layer thickness and nature of internal and outer contacts. Lateral changes are remarkably insignificant over >4 km of exposure. Sedimentary features such as cross-bedding, channels and flame structures are rare, but occasionally observed closer to the margins (Lindhuber *et al.*, 2015). The layering dips gently towards the center of the complex, steepens towards the margin (Fig. 3), and fades against a marginal pegmatite zone comprising a kakortokite-like matrix with densely intersecting pegmatite veins. The marginal pegmatite decreases in width from 100 m at the lowermost exposed levels to *c.* 25 m at higher levels. Metre-scale autoliths of naujaite and augite syenite are entrained in unit +3, slightly compressing the underlying unit and, in turn, gently draped by the overlying unit (Figs 2 and 3). Parts of the LLK are cut by a chaotic mass of fine-grained mesocratic rocks, originally termed 'slumped' kakortokites (Bohse *et al.*, 1971), but now described as 'hybrids' representing mixtures of less evolved Ti-rich melts with kakortokite mush (Hunt, 2015). The uppermost LLK unit (+17) grades into the *c.* 50 m thick SLK sequence, which has not been studied in detail due to poor exposure and severe alteration.

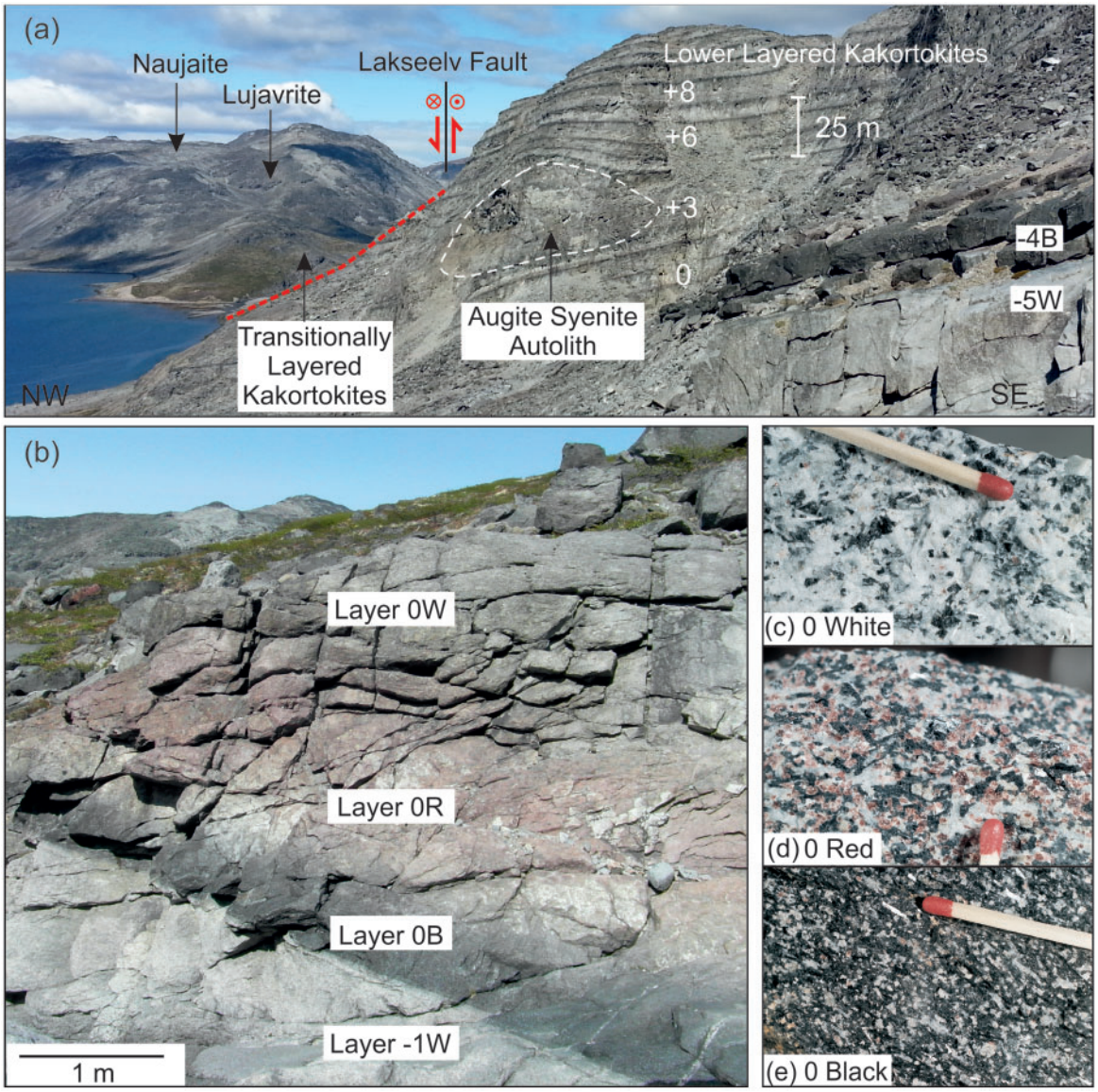

Fig. 2. (a) Field relations in the southern part of the Ilímaussaq complex. Lower layered kakortokites (LLK) are visible in the foreground, enveloping a large autolith of augite syenite in unit +3. Note sharp contact between unit -5 W and overlying unit -4B in lower right corner (note scale change due to oblique view). Far left: overlying lujavrites (dark) intrude the naujaite roof sequence (light grey). North-block down movement along the Lakseelv fault exposed the LLK against the higher level transitional layered kakortokites (TLK) and lujavrites. (b)–(e) Key outcrop of marker horizon unit 0 in the Laksetværelv valley, with close-ups of 0 W, 0 R and 0B in hand sample (from Sørensen *et al.*, 2006*b*) illustrating the variations in modal arfvedsonite (black), EGM (red), alkali feldspar (white) and nepheline (grey), respectively. Note gradual internal transitions between black, red and white layers and sharp boundary between the black base of unit 0 and the underlying white kakortokite of unit -1. Match-tip is 5 mm.

The TLK (*c.* 60 m) are exposed north of the Lakseelv valley (Figs 1 and 2), and exhibit modal layering comparable to the LLK, albeit less pronounced and systematic. They are inferred to overly the SLK by means of a large E–W hinge-fault through the Lakseelv valley (Bohse *et al.*, 1971). Maximum vertical displacement along the fault is estimated between 350 and 600 m (north-block down) at the head of Kangerluarsuk, decreasing towards the northeast (Bohse & Andersen, 1981). The TLK are labelled from I to A upwards, with letters instead of numbers referring to their ambiguous stratigraphic relation to the LLK and SLK south of the fault. The TLK evolve upwards into aegirine-dominated (green) lujavrites, in which the uppermost transitional kakortokite (unit A) is marked by an aegirine-rich, rather than an arfvedsonite-rich base.

The aegirine lujavrite is divided into aegirine lujavrite I (*c.* 70 m thick) and overlying aegirine lujavrite II (*c.* 100 m thick), the latter being finer grained and paler green in outcrop (Bohse & Andersen, 1981; Bailey, 1995). Aegirine lujavrite II is intruded by a sheet of arfvedsonite lujavrite (A) with sharp intrusive contacts and more primitive EGM compositions (Ratschbacher *et al.*, 2015). The lujavrites show strong foliation fabrics, draping autoliths and following intrusive contacts, and occasional cryptic- and microrhythmic modal layering

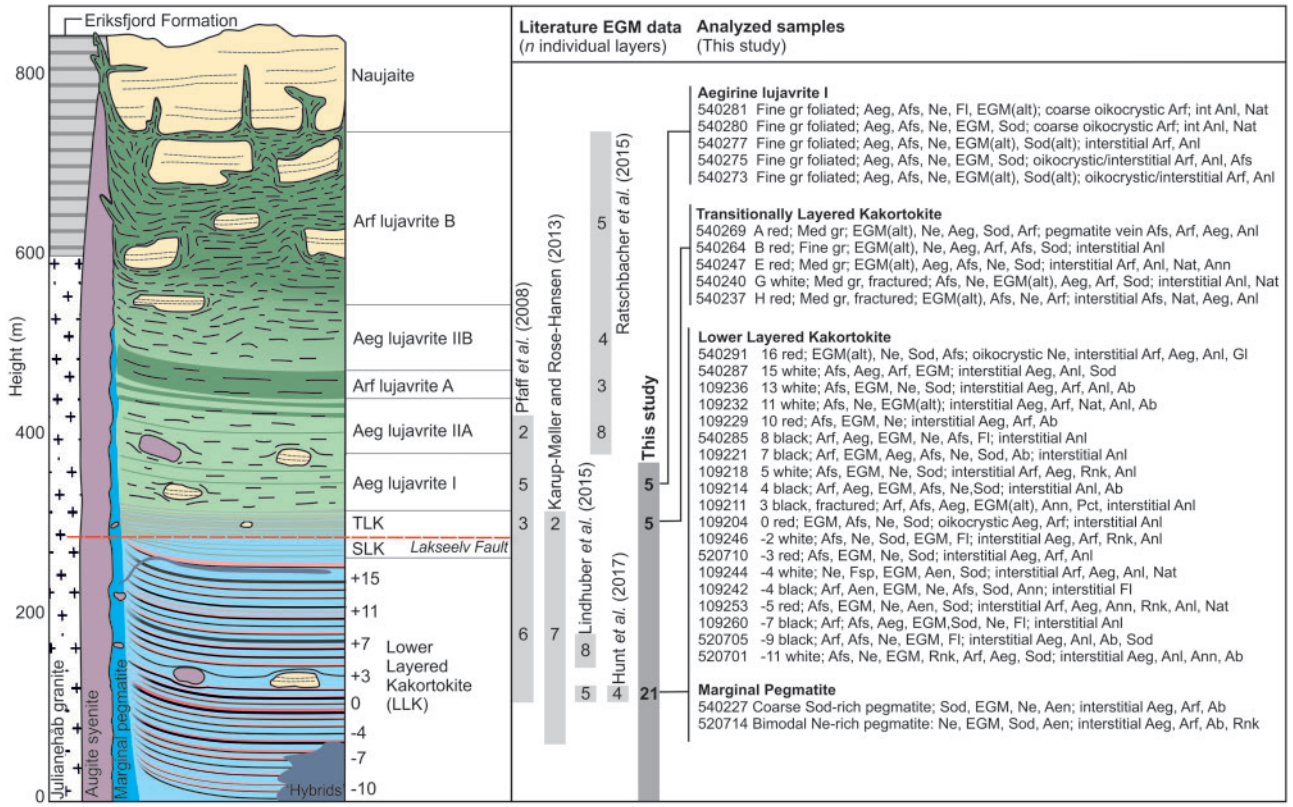

Fig. 3. Schematic cross-section of the kakortokite-lujavrite sequence (modified after Andersen *et al.*, 1981), with stratigraphic coverage of EGM data available in the literature and list of analyzed samples in this study. First mineral listed is dominant. See Table 1 for mineral abbreviations.

(e.g. Bailey *et al.*, 2006). The most evolved lujavritic melts are characterized by hyperagpaitic mineral assemblages, e.g. containing steenstrupine-(Ce) instead of EGM and naujakasite instead of nepheline (e.g. Sørensen & Larsen, 2001; Andersen & Sørensen, 2005; Andersen & Friis, 2015). In this work, only the lower section of aegirine lujavrite I is considered (Fig. 3). More detailed petrographic and structural descriptions of the lujavrites are given by Ratschbacher *et al.* (2015).

PETROGRAPHY

Samples were collected from various locations along the Kringlerne coast, plateau and Lakseelv valley in 2013 (Fig. 1), supplemented with samples from the original mapping collection of Bohse *et al.* (1971) stored in Copenhagen archives, to generate a complete set of black, red and white layers across the sequence. Samples with low degrees of EGM alteration (Borst *et al.*, 2016), selected to cover the full LLK sequence (unit -11 to +16) were selected for analysis (n = 31), including six black, five red and seven white kakortokites, five transitional kakortokites, five aegirine lujavrite I and two marginal pegmatites (Fig. 3).

The kakortokites are dominated by arfvedsonitic amphibole, alkali feldspar, nepheline, EGM and sodalite in differing proportions (Fig. 4). Alkali feldspar is bimodal, mostly forming coarse laths (up to 6 mm) of exsolved or tiled, simple twinned and partly albitized perthite, or interstitial clusters of albite laths (0·2 – 0·5 mm). Aegirine, aenigmatite, rinkite, fluorite and analcime are minor phases, and vary in modal abundance from unit to unit as well as between black, red and white layers. Accessory minerals include (fluor-) apatite, as inclusions in arfvedsonite (Fig. 4c) and aegirine, or in EGM alteration assemblages, sphalerite, galena and thorite. Autometasomatism is expressed by partial replacement of sodalite, nepheline and alkali feldspar by zeolites (analcime and natrolite, Fig. 4a), arfvedsonite and aenigmatite by secondary aegirine and occasionally annite, and EGM by phases such as catapleiite, zircon, gittinsite, aegirine, nacareniobsite-(Ce), monazite-(Ce), britholite-(Ce) and A1-minerals (Table 1; Karup-Møller *et al.*, 2010; Karup-Møller & Rose-Hansen, 2013; Borst *et al.*, 2016).

Black and white kakortokites exhibit stratiform lamination of amphibole and/or alkali feldspar. Red kakortokites are typically saccharoidal with less prominent lamination. Arfvedsonite occurs as a euhedral cumulus phase (0·2–5 mm) in the black kakortokites (Fig. 4c), while more commonly occurring interstitially in the red and white kakortokites (Fig. 4a, b). Aegirine texturally resembles arfvedsonite and is more abundant in the upper LLK and TLK, eventually replacing arfvedsonite as the dominant Fe-phase in the upper TLK and aegirine lujavrites (Fig. 4e, f).

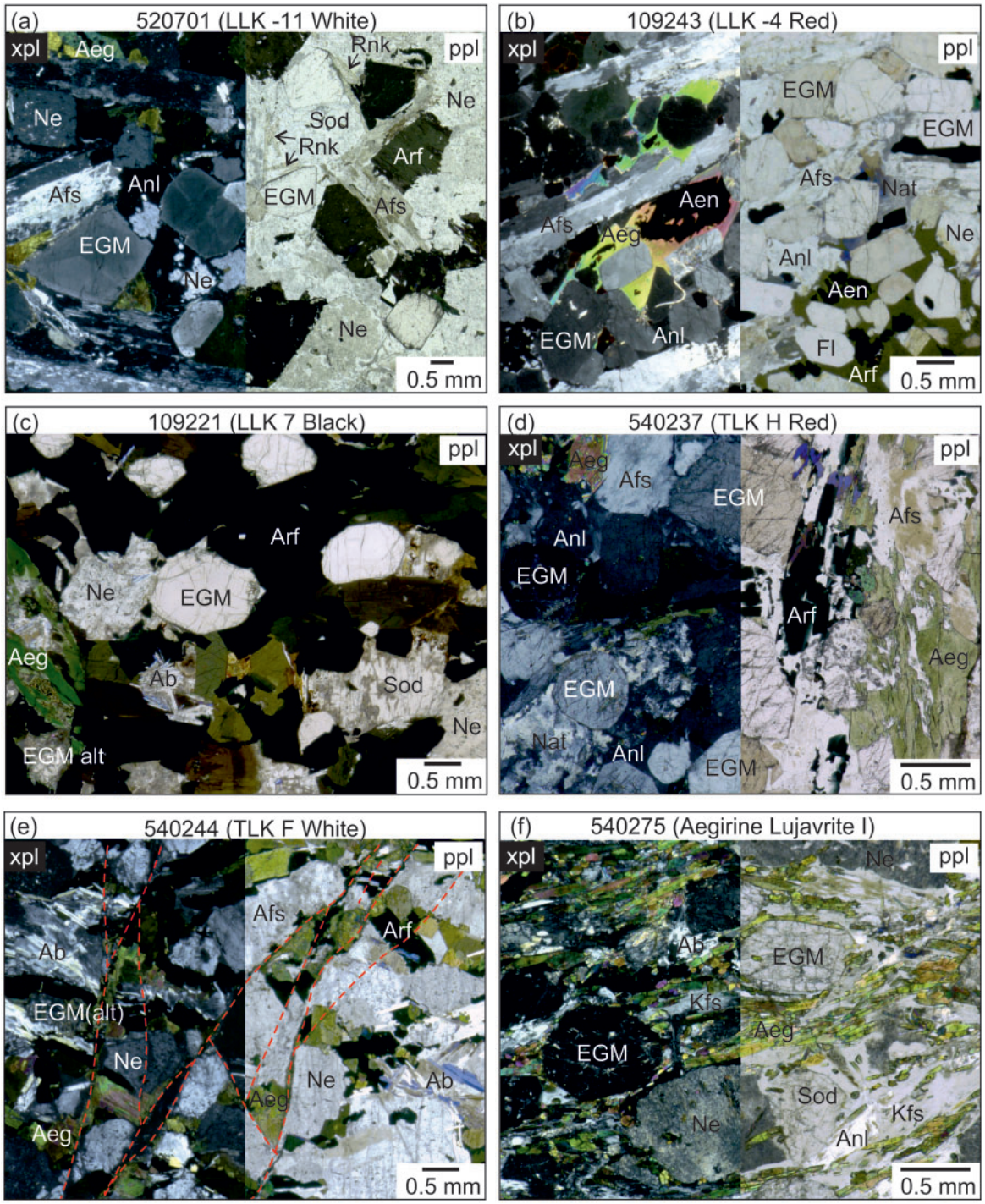

Fig. 4. Thin section photographs in plane polarized (ppl) and cross polarized light (xpl). (a) Layer -11 W containing subhedral zoned EGM, simple twinned alkali feldspar laths, yellow rinkite prisms and equant nepheline partially replaced by analcime. Arfvedsonite (army-green to black) and aegirine (grass-green) occur interstitially. (b) Layer -4 R rich in euhedral EGM, red-brown aenigmatite, nepheline, elongate twinned alkali feldspar, with interstitial arfvedsonite, aegirine, natrolite and analcime. (c) Interlocked arfvedsonite crystals surrounding equant nepheline, sodalite (replaced by analcime) and EGM (partially altered). (d) Layer H Red of TLK. Note textural similarity to red kakortokite in LLK, with dominance of aegirine over arfvedsonite. (e) Brittle micro-fractures (red lines) in F White, from the Lakseelv fault zone. Equant nepheline and EGM are enveloped by aegirine and alkali feldspar laths, defining a weak magmatic lamination perpendicular to the micro-fractures. Note pockets of albite laths. (f) Fine-grained, foliated aegirine lujavrite I. Foliation defined by prismatic aegirine and interstitial alkali feldspar, analcime and natrolite wrapped around equant nepheline (replaced by analcime), sodalite, and EGM.

Eudialyte-group minerals occur euhedrally in all layers and range in size between 0·5 and 4 mm in the LLK, decreasing to c. 0·3–1 mm in the TLK and aegirine lujavrites. They commonly comprise a euhedral sector-zoned core, occasionally with μm-scale oscillatory zoning and concentric, subhedral overgrowths (Figs 4 and 5). Rinkite (sub- to euhedral, Fig. 5e, f, l) and aenigmatite (sub- to euhedral) are common accessories in the lower part of the LLK, particularly in unit -4 (Fig. 4b), but are rare to absent in the TLK and aegirine lujavrites.

The upper TLK and aegirine lujavrites exhibit a bimodal grain size distribution, containing c. 0·5–1 mm primocrysts of nepheline, EGM and sometimes alkali feldspar and sodalite, enveloped by finer prismatic aegirine and albite laths (Fig. 4f). The lujavrites contain separate (i.e. subsolvus) albite and microcline laths as opposed to coarse patch perthites in the kakortokites. The lujavrites exhibit pronounced magmatic fabrics such as foliation, lineation and sometimes C′-type shear bands (Fig. 4f, see Ratschbacher *et al.*, 2015). Transitional kakortokites near the Lakseelv fault additionally show brittle–ductile deformation features with microscopic fractures crosscutting primary minerals and recrystallized aegirine-II along shear planes (Fig. 4e).

ANALYTICAL METHODS

Compositional analyses of EGM were performed at the Department of Geosciences, University of Oslo, using a CAMECA SX100 electron microprobe (EMP) fitted with five wavelength-dispersive spectrometers (WDS). An acceleration voltage of 15 kV, beam current of 15 nA and defocused beam of 25 μm were used to avoid Na migration and minimize beam damage effects (Atanasova *et al.*, 2015). Sodium, Zr, Si and Cl were measured first and X-ray counts were monitored for in-run signal stability. Calibration standards used and corrections applied are as described in Borst *et al.* (2016). Eudialyte of a known composition (Kipawa complex, Johnsen & Gault, 1997) was analyzed during each session for external control. Qualitative element maps were produced using a JEOL JXA8200 EPMA at the Department of Geosciences and Natural Resource Management, University of Copenhagen, in WDS mode using a pixel size of 3 μm, an overlapping beam size of 5 μm and 200 ms counting time per pixel. For each sample two to six EGM grains with well-developed sector zoning and/or overgrowths were selected for analyses. Samples were analyzed in random stratigraphic order. A total of 690 analyses yielded average compositions for 136 individual sectors and 63 overgrowths from 25 kakortokites and 6 lujavrites (Supplementary Data SI; supplementary data are available for downloading at http://www.petrology.oxfordjournals.org).

Formulae were calculated based on (Si + Zr + Ti + Nb + Al + Hf) = 29 apfu (Johnsen & Grice, 1999) and cations assigned to structural sites following the guidelines of Johnsen *et al.* (2003) and Pfaff *et al.* (2010), implementing suggestions by Andersen *et al.* (2010). For consistency with previous work (e.g. Pfaff *et al.*, 2008; Lindhuber *et al.*, 2015; Hunt *et al.*, 2017), and due to the subjective nature of the cation site assignment procedure, data are presented as total apfu and ratios only. We observe that if data are presented based on assigned site occupancies, potentially misleading trends are introduced. For example, for analyses where Fe is >3 (on M2), the remaining Fe and Mn are assigned to the M1-site. The M1 site is then filled to six with Ca. Subsequently, all REE are assigned to the N-site, which suggests that the sample is REE poor when visualizing only the M1-assigned Ca/(REE + Y) ratios. Similarly, when Zr + Hf <3, Nb is needed to fill the Z-site, giving the impression that the sample is Nb poor when visualizing M3-site assigned Nb.

Trace elements were analyzed using laser-ablation inductively coupled plasma mass spectrometry (LA-ICP-MS) at the Geological Survey of Denmark and Greenland. The system uses a UP 213 frequency-quintupled Nd: YAG solid state laser system (New Wave Research) coupled to an Element 2 sector-field ICP-MS (Thermo-Fisher Scientific). Data were acquired using a laser diameter of 40 μm, a nominal laser fluence of 10 J/cm^2 and a pulse rate of 5 Hz. Total acquisition time was 90 s per analysis, including 30 s for gas blank and background, 30 s for laser ablation and 30 s for washout. Offline data reduction was performed using Iolite 2.5 (Paton *et al.*, 2011) using ^{42}Ca as the internal standard element, determined by EMP. Instrumental drift was monitored by measuring NIST612, NIST614 and BHVO-2, bracketing every eight sample analyses. External standard measurements were controlled by the BHVO-2 and NIST614 glass reference standards, yielding internal 2SE precision and accuracy within 10% for all elements measured. Average detection limits were between 0·002 and 0·6 ppm, except for Ti and Zr with detection limits of *c.* 1·5 and 2·1 ppm, respectively (Supplementary Data SII). Approximately 3–4 grains per sample and, depending on the size, 3–8 spots per crystal were analyzed, yielding 148 spots and 21 core–rim traverses in total.

RESULTS

We describe EGM compositions in terms of cores and overgrowths to identify crystal-scale, unit-scale and sequence-scale fractionation trends. To gain insight into melt evolution, we first identify crystallographically controlled heterogeneities that are independent of magma evolution (i.e. sector zoning). Within the euhedral cores of EGM, three types of zoning are identified: (i) sector zoning, (ii) oscillatory zoning and (iii) core to rim zoning (Fig. 5). In addition, we distinguish two types of EGM overgrowths which exhibit either relatively dark or bright backscatter electron (BSE) intensities compared to cores (Fig. 5a, b). Stratigraphic variations in average compositions of cores and overgrowths are

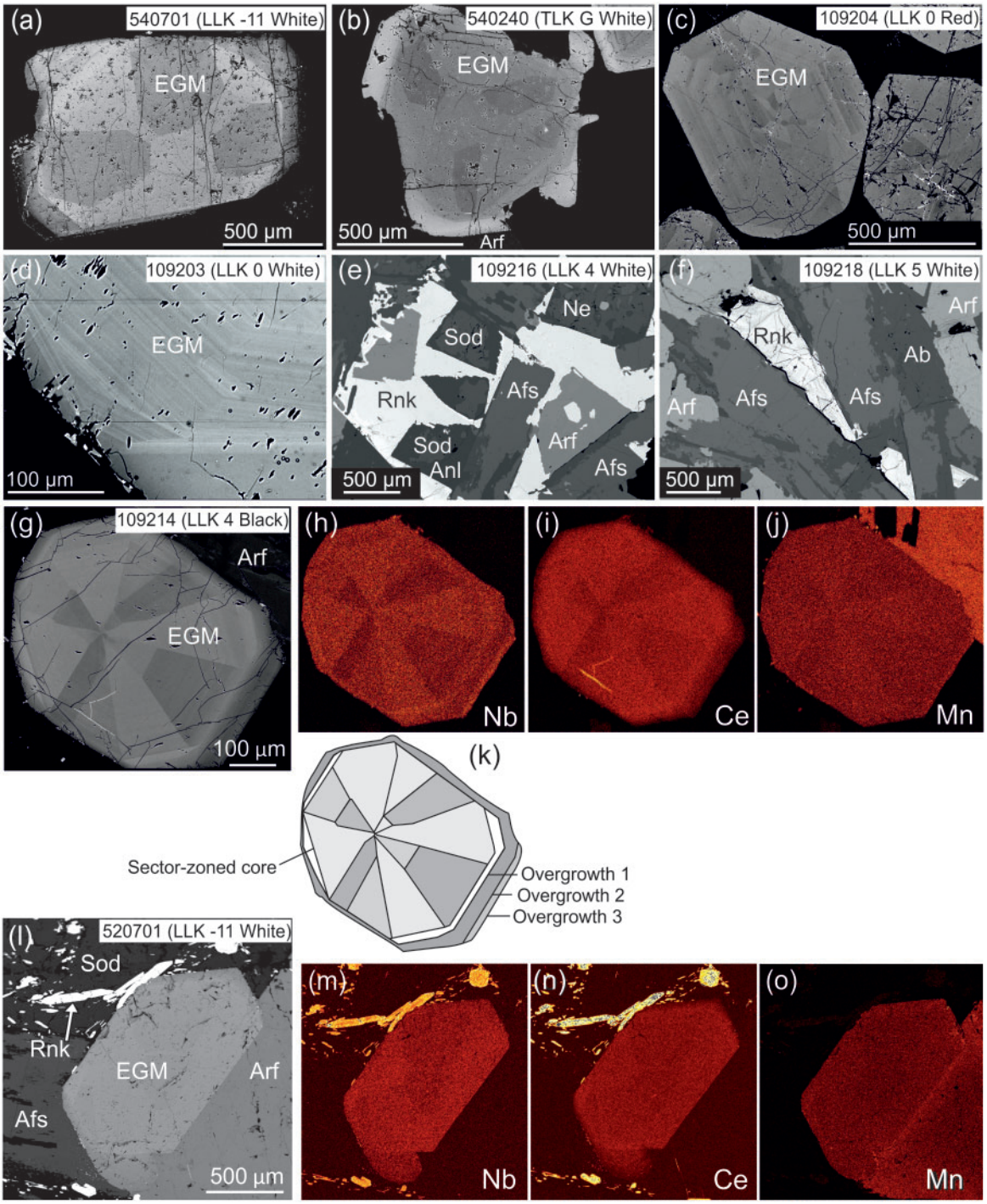

Fig. 5. Backscattered electron (BSE) images and elemental maps illustrating EGM zoning patterns and rinkite textures. (a)-(b) Subhedral EGM with euhedral sector-zoned core (oriented perpendicular to the c-axis) with BSE-dark and BSE-bright irregular overgrowths. (c) Euhedral EGM with complex sector- and oscillatory zoning, no overgrowths. Oscillatory zoning shows multiple 'normal' zoning cycles, i.e. from dark to bright in BSE. Adjacent EGM are cracked and partially replaced. (d) Oscillatory zoned (<2–5 μm) EGM core with oscillation-free overgrowth (bottom). (e) Rinkite enclosing alkali feldspar (Afs), arfvedsonite, nepheline (Ne) and sodalite, partly altered to analcime (Anl). (f) Interstitial rinkite between alkali feldspar (K-feldspar cores with turbid albite rims) and arfvedsonite. (g) Sector-zoned EGM crystal with multiple overgrowths with (h)-(j) qualitative EMP element maps for Nb, Ce and Mn and (k) annotated sketch. Grain oriented approximately parallel to *c*-axis, with the *c*-axis normal to elongate crystal faces (lower left to upper right). Partial overgrowth (1) with elevated REE and Nb, followed by overgrowths with (2) low Nb and REE and (3) high Nb–Mn, low REE. (l) Euhedral EGM surrounded by perthitic feldspar (Afs), arfvedsonite (Arf), sodalite (Sod), and clusters of prismatic rinkite (Rnk) along grain boundaries, (m-o) element maps for Nb, Ce and Mn. Late-stage EGM growth formed a partial rim (upper face) and epitaxial lobe (lower face) with lower REE and Nb contents (dark in BSE).

Table 2: Representative EMP data for EGM sectors and overgrowths

Sample	540 214			520 701		520 705				109 214			
Unit	Marginal Pegmatite			LLK -11 White		LLK -9 Black				LLK 4 Black			
Domain[a]	bs	ds	do	bs	ds	bs	ds	bo	do	bs	ds	bo	bo
n[b]	4	3	3	4	4	4	4	3	2	5	5	5	3
(wt %)													
Na_2O[b]	13·68	13·88	13·71	14·05	14·01	13·86	13·82	13·65	13·64	13·74	13·93	13·38	13·32
Al_2O_3	0·21	0·25	0·15	0·25	0·26	0·22	0·28	0·23	0·20	0·20	0·24	0·21	0·21
SiO_2	47·70	48·07	49·76	48·04	48·17	48·30	48·24	48·21	48·89	48·41	48·08	48·35	47·89
Cl	1·67	1·66	0·99	1·62	1·60	1·62	1·59	1·49	1·15	1·53	1·49	1·34	1·42
K_2O	0·29	0·29	0·25	0·31	0·28	0·27	0·26	0·27	0·25	0·31	0·30	0·27	0·26
CaO	11·03	10·89	11·01	10·68	10·59	10·52	10·66	10·60	10·60	10·53	10·67	10·57	10·53
FeO	6·12	6·13	6·32	6·05	6·30	6·37	6·36	6·07	6·41	6·31	6·33	6·28	6·23
MnO	0·79	0·71	0·54	0·80	0·77	0·67	0·61	0·61	0·53	0·67	0·62	0·49	0·67
Y_2O_3	0·39	0·38	0·22	0·42	0·41	0·43	0·39	0·42	0·35	0·48	0·43	0·47	0·45
ZrO_2	11·51	11·45	11·66	11·36	11·42	11·56	11·72	11·64	11·67	11·08	11·11	11·06	10·96
Nb_2O_5	1·36	0·98	0·45	1·14	0·86	1·04	0·84	1·09	0·71	0·95	0·80	0·79	1·09
La_2O_3	0·55	0·42	0·28	0·50	0·42	0·45	0·42	0·55	0·32	0·47	0·44	0·47	0·56
Ce_2O_3	0·95	0·82	0·35	0·98	0·88	0·91	0·84	1·04	0·59	0·94	0·89	0·91	1·17
Nd_2O_3	0·38	0·29	0·05	0·36	0·36	0·35	0·40	0·39	0·24	0·34	0·35	0·38	0·42
HfO_2	0·24	0·28	0·17	0·25	0·26	0·21	0·25	0·24	0·17	0·22	0·25	0·22	0·26
TiO_2	0·08	0·07	0·08	0·07	0·07	0·06	0·07	0·04	0·06	0·06	0·06	0·04	0·03
Cl=O	0·38	0·38	0·22	0·37	0·36	0·37	0·36	0·34	0·26	0·34	0·34	0·30	0·32
Total	96·66	96·32	95·72	96·51	96·30	96·60	96·56	96·27	95·59	95·87	95·66	94·94	95·13
Formulae based on (Si, Zr, Ti, Nb, Al, Hf) = 29													
Na	14·17	14·32	13·78	14·49	14·43	14·23	14·18	14·03	13·89	14·16	14·43	13·82	13·85
Al	0·13	0·16	0·09	0·16	0·16	0·13	0·17	0·14	0·12	0·12	0·15	0·13	0·13
Si	25·47	25·57	25·80	25·56	25·61	25·58	25·53	25·54	25·67	25·72	25·69	25·76	25·69
Cl	1·51	1·50	0·87	1·46	1·45	1·46	1·42	1·34	1·02	1·37	1·35	1·21	1·29
K	0·20	0·19	0·16	0·21	0·19	0·18	0·18	0·18	0·17	0·21	0·21	0·19	0·18
Ca	6·31	6·21	6·12	6·08	6·03	5·97	6·05	6·02	5·96	6·00	6·11	6·03	6·05
Fe	2·73	2·73	2·74	2·69	2·80	2·82	2·81	2·69	2·81	2·80	2·83	2·80	2·79
Mn	0·36	0·32	0·24	0·36	0·34	0·30	0·28	0·28	0·23	0·30	0·28	0·22	0·31
Y	0·11	0·11	0·06	0·12	0·12	0·12	0·11	0·12	0·10	0·13	0·12	0·13	0·13
Zr	3·00	2·97	2·95	2·95	2·96	2·98	3·03	3·01	2·99	2·87	2·90	2·87	2·87
Nb	0·33	0·24	0·11	0·27	0·21	0·25	0·20	0·26	0·17	0·23	0·19	0·19	0·26
La	0·11	0·08	0·05	0·10	0·08	0·09	0·08	0·11	0·06	0·09	0·09	0·09	0·11
Ce	0·19	0·16	0·07	0·19	0·17	0·18	0·16	0·20	0·11	0·18	0·17	0·18	0·23
Nd	0·07	0·05	0·01	0·07	0·07	0·07	0·07	0·07	0·05	0·06	0·07	0·07	0·08
Hf	0·04	0·04	0·03	0·04	0·04	0·03	0·04	0·04	0·03	0·03	0·04	0·03	0·04
Ti	0·03	0·03	0·03	0·03	0·03	0·02	0·03	0·02	0·02	0·02	0·02	0·02	0·01
O	76·16	75·90	74·79	75·99	75·89	75·76	75·68	75·57	75·05	75·74	75·91	75·41	75·70
Sum	53·25	53·17	52·23	53·31	53·24	52·95	52·92	52·70	52·39	52·94	53·30	52·53	52·73
∑(REE+Y)	0·48	0·40	0·19	0·48	0·44	0·45	0·43	0·50	0·32	0·47	0·45	0·48	0·55

(continued)

summarized in Figure 7 and representative data are given in Table 2.

Sector zoning

Sector zoning is observed in most EGM crystals under crossed polarizers (Fig. 4a, b) and in backscattered electron images (Fig. 5). EGM crystals oriented along the crystallographic *c*-axis show flattened octagonal habits with four individual BSE-dark sectors (Fig. 5g–k), while grains perpendicular to the *c*-axis (Fig. 5a, b) show pseudo-hexagonal habits with three dark sectors around a central nucleus. Qualitative element maps reveal minor sectoral variations in Nb, REE + Y and Mn (Fig. 5g–o). On average, BSE-bright sectors contain *c.* 0·05 apfu more Nb, and *c.* 0·02 to 0·06 apfu more REE + Y than BSE-dark sectors (Table 2; Figs 6 and 7). Mn contents are also marginally elevated (*c.* 0·03 apfu) in BSE-bright sectors, associated with lower Fe/Mn ratios (Fig. 7a). Sectoral variations in other elements, e.g. lower Al/Si and Zr/Hf for bright sectors, are also identified but less pronounced. Sector zoning is commonly attributed to differential incorporation of cations on non-equivalent crystal faces exhibiting different site arrangements and lattice point densities, depending on the orientation at which they truncate the crystal lattice (e.g. Dowty, 1976; Reeder & Rakovan, 1999). In the example shown in Figure 5k, high Nb–REE sectors indicate growth along faces oriented at an angle to the *c*-axis (e.g. {10$\bar{1}$1}, {0$\bar{1}$12}), i.e. faces with lower lattice point densities, whereas low Nb–REE sectors develop from faces normal or parallel to the *c*-axis (e.g. {0001}, {10$\bar{1}$0}, {11$\bar{2}$0}), i.e. higher lattice point densities, Johnsen & Grice, 1999. It is possible that face-specific partitioning

Table 2: Continued

Sample	109 236			540 240			540 269			540 277		
Unit	LLK 13 White			TLK G White			TLK A Red			Aegirine Lujavrite I		
Domain[a]	bs	ds	bo	bs	ds	bo	bs	ds	bo	bs	ds	bo
n[b]	4	3	2	6	3	4	4	3	2	5	3	4
(wt %												
Na_2O[b]	13·17	13·21	7·06	13·72	13·91	11·77	13·12	13·36	11·48	13·21	13·53	12·98
Al_2O_3	0·26	0·27	0·33	0·21	0·27	0·17	0·20	0·22	0·09	0·20	0·20	0·16
SiO_2	48·99	48·96	50·03	48·70	49·12	47·32	48·90	49·33	48·79	48·25	48·60	47·69
Cl	1·44	1·38	0·98	1·32	1·23	0·92	1·15	1·16	0·44	0·99	0·99	0·89
K_2O	0·27	0·25	0·38	0·24	0·26	0·31	0·46	0·45	0·79	0·42	0·35	0·40
CaO	9·85	9·84	9·92	9·48	9·49	8·93	9·04	9·12	8·93	7·98	8·45	8·00
FeO	5·51	5·56	5·54	6·21	6·21	5·55	5·75	5·96	5·40	4·80	4·96	4·53
MnO	0·80	0·78	0·88	0·92	0·88	1·17	1·08	1·01	1·29	1·42	1·40	1·51
Y_2O_3	0·46	0·46	0·69	0·48	0·45	0·83	0·58	0·56	0·62	0·84	0·82	0·89
ZrO_2	10·86	10·87	10·79	11·71	11·93	11·50	11·73	11·68	11·37	12·00	11·91	11·53
Nb_2O_5	0·79	0·55	1·09	0·72	0·57	1·72	0·81	0·56	1·27	0·94	0·63	1·08
La_2O_3	0·49	0·47	0·78	0·48	0·41	1·18	0·57	0·51	0·92	0·80	0·65	1·19
Ce_2O_3	0·93	0·92	1·43	0·99	0·84	2·10	1·26	1·03	1·92	1·64	1·44	2·38
Nd_2O_3	0·39	0·36	0·44	0·45	0·47	0·80	0·58	0·45	0·74	0·74	0·72	1·06
HfO_2	0·22	0·26	0·15	0·18	0·19	0·14	0·19	0·17	0·17	0·18	0·17	0·16
TiO_2	0·04	0·04	0·04	0·05	0·06	0·04	0·03	0·03	0·04	0·03	0·03	0·03
Cl=O	0·32	0·31	0·22	0·30	0·28	0·21	0·26	0·26	0·10	0·22	0·22	0·20
Total	94·15	93·88	90·30	95·59	96·11	94·38	95·62	95·46	94·22	94·37	94·82	94·62
Formulae based on (Si, Zr, Ti, Nb, Al, Hf) = 29												
Na	13·45	13·52	7·05	14·03	14·06	12·26	13·34	13·51	11·72	13·54	13·83	13·50
Al	0·16	0·17	0·20	0·13	0·16	0·11	0·12	0·13	0·05	0·13	0·13	0·10
Si	25·81	25·85	25·80	25·64	25·62	25·42	25·64	25·73	25·69	25·51	25·63	25·58
Cl	1·28	1·23	0·86	1·18	1·09	0·84	1·03	1·03	0·40	0·88	0·89	0·81
K	0·18	0·17	0·25	0·16	0·18	0·21	0·31	0·30	0·53	0·28	0·23	0·28
Ca	5·56	5·57	5·48	5·35	5·30	5·14	5·08	5·10	5·04	4·52	4·77	4·60
Fe	2·43	2·46	2·39	2·73	2·71	2·49	2·52	2·60	2·38	2·12	2·19	2·03
Mn	0·36	0·35	0·38	0·41	0·39	0·53	0·48	0·45	0·57	0·64	0·63	0·69
Y	0·13	0·13	0·19	0·13	0·13	0·24	0·16	0·15	0·17	0·24	0·23	0·26
Zr	2·79	2·80	2·71	3·01	3·03	3·01	3·00	2·97	2·92	3·09	3·06	3·02
Nb	0·19	0·13	0·25	0·17	0·13	0·42	0·19	0·13	0·30	0·22	0·15	0·26
La	0·10	0·09	0·15	0·09	0·08	0·23	0·11	0·10	0·18	0·16	0·13	0·24
Ce	0·18	0·18	0·27	0·19	0·16	0·41	0·24	0·20	0·37	0·32	0·28	0·47
Nd	0·07	0·07	0·08	0·08	0·09	0·15	0·11	0·08	0·14	0·14	0·14	0·20
Hf	0·03	0·04	0·02	0·03	0·03	0·02	0·03	0·03	0·03	0·03	0·03	0·02
Ti	0·02	0·02	0·02	0·02	0·03	0·02	0·01	0·01	0·01	0·01	0·01	0·01
O	74·53	74·52	71·39	74·95	74·72	74·54	74·39	74·36	73·73	73·96	74·23	74·43
Sum	51·45	51·53	45·25	52·18	52·09	50·68	51·35	51·49	50·10	50·95	51·42	51·26
∑(REE+Y)	0·47	0·47	0·69	0·50	0·45	1·04	0·62	0·53	0·86	0·85	0·77	1·16

[a]bs, BSE-bright sector; ds, BSE-dark sector; do, BSE-dark overgrowth; bo, BSE-bright overgrowth.
[b]Number of analyses per domain. Mean values of all analysed EGM domains, including 2σ values in wt % and apfu, are given in Supplementary Data SI.

mainly affected the high charge HFSE group (e.g. Nb, REE, Y and Hf), while sectoral variations in Mn, Fe and Al are related to substitutional and charge-balance mechanisms imposed by the former. Important for this work is that the sectoral variations are consistent across the sequence and can thus readily be distinguished from magmatic fractionation trends.

Oscillatory zoning

Some EGM cores exhibit μm-scale oscillatory zoning (Fig. 5d). Individual oscillations are too thin (<5 μm) to analyze quantitatively, given the required beam size of 25 μm Nevertheless, the patterns illustrate that EGM maintained euhedral shapes throughout much of their growth history, at least during crystallization of the sector-zoned cores.

Core to rim trends within euhedral cores

Traverses across EGM crystals show minor core-to-rim variations within their euhedral sector-zoned cores. Some EGM crystals reveal increasing REE + Y contents towards the outer part of the cores (Fig. 6, up to 20%). Chlorine contents are constant across most EGM cores, but occasionally decrease towards the margin of the core before significantly decreasing in the overgrowths (see below) (Fig. 6). No systematic core to rim trends are observed for Nb and Fe/Mn ratios, which mostly vary across sector boundaries (Fig. 6).

Table 3: LA-ICPMS data for selected EGM grains

Sample	109203								109244							
Unit	0 White (Grain nr. 1)								-4 White (Grain nr. 1, Fig. 9, 10a)							
Domain[a]	r	c	c	c	c	c	r	bo	r	c	c	c	c	c	do	bo
Trace elements (ppm)																
Ti	225	343	311	335	307	320	253	292	368	370	405	408	372	371	362	518
Rb	11·0	12·1	13·7	13·0	15·0	13·2	9·5	10·8	13·8	14·4	15·7	15·3	15·1	14·8	14·0	16·8
Sr	875	796	688	810	751	669	596	640	709	664	689	701	676	692	403	457
Ba	1030	730	576	634	568	717	730	760	852	606	659	648	683	809	660	1470
La	4370	4630	3790	4350	4120	4200	3710	4030	4710	4330	4650	4660	4350	4890	5820	9840
Ce	6520	7800	5850	7540	6620	7240	6340	6300	7280	6430	6770	6930	6870	7810	8650	13360
Pr	834	900	780	843	791	905	820	835	878	776	823	809	806	949	1003	1453
Nd	3620	3560	3120	3520	3300	3450	3570	3690	3570	3330	3310	3410	3350	3740	4060	5700
Sm	753	769	701	727	730	749	801	911	764	719	684	678	668	764	848	1163
Eu	68·1	67·5	61·0	64·0	64·5	66·7	66·5	61·4	62·5	59·2	59·7	61·6	60·8	70·3	73·2	94·0
Gd	833	840	776	806	798	794	951	989	751	728	679	684	686	699	804	1118
Tb	145	140	140	143	146	134	163	168	132	133	127	130	125	129	143	190
Dy	991	991	972	965	1010	954	1112	1170	991	984	958	961	945	962	970	1392
Ho	224	217	235	227	231	221	246	233	210	202	207	201	201	206	206	287
Er	664	665	686	609	664	621	686	635	617	646	639	622	619	651	596	884
Tm	101	106	109	97	105	99	107	100	100	101	105	103	99	103	97	144
Yb	724	750	730	680	714	687	740	687	630	663	685	673	695	689	628	977
Lu	80·5	80·0	79·0	78·2	79·3	78·0	81·0	77·4	70·5	71·2	74·7	72·5	71·5	73·6	66·3	105
Y	4910	4770	5320	4740	5150	4660	5710	5510	4560	4590	4520	4440	4390	4540	4690	9300
Hf	2690	2330	2510	2250	2390	2510	2190	1790	2040	1990	2270	2250	2280	2280	2290	1096
Nb	7700	6280	6100	6540	6000	5530	5670	4280	7130	7100	8190	7710	7100	7160	6060	10170
Ta	910	690	538	739	638	551	538	312	957	934	997	1010	907	960	699	448
Pb	57·7	80·5	63·3	77·8	71·6	62·3	43·3	42·0	75·7	87·5	94·1	104	87·4	74·1	52·3	249
Th	24·2	19·7	17·3	18·3	17·3	16·7	14·2	15·7	16·6	15·9	16·7	17·2	16·7	18·2	19·5	119
U	19·0	34·0	23·6	32·2	27·5	24·9	22·5	20·3	21·3	23·4	24·7	26·8	25·9	26·7	30·7	309

Sample	520701								520701							
Unit	-11 White (Grain nr· 1, Fig· 10b)								-11 White (Grain nr· 3, Fig· 10c)							
Domain[a]	do	r	c	c	c	c	bo	do	do	c	c	c	c	r	do	do
Trace elements (ppm)																
Ti	344	326	368	359	370	379	409	348	387	365	405	374	394	310	452	267
Rb	7·4	16·6	16·9	15·0	16·8	16·6	11·0	8·1	11·8	16·1	17·8	16·9	17·4	12·2	9·4	12·5
Sr	406	1032	905	796	802	826	1014	714	724	808	787	635	845	820	760	1143
Ba	492	910	487	483	605	491	1180	851	775	412	358	312	656	977	1076	1411
La	2310	4570	3970	3790	4040	4010	5130	3680	3830	4190	4160	3810	4310	4830	3090	3150
Ce	2680	7460	6610	6240	6370	6250	7500	5110	4970	6340	6540	5710	7010	7130	3150	3460
Pr	271	873	820	742	784	798	990	604	599	801	794	722	823	842	327	393
Nd	957	3410	3210	3050	3140	3050	3530	2490	2180	2830	2910	2720	3060	3106	1160	1490
Sm	192	695	663	649	651	683	733	624	564	644	662	635	685	716	284	463
Eu	17·5	62·3	57·7	59·2	58·8	55·4	68·4	44·7	41·4	57·9	54·7	54·8	59·2	58·0	22·5	34·7
Gd	250	772	724	766	721	716	741	754	659	742	733	720	762	748	365	583
Tb	45·8	132·5	126·8	127·8	119·9	122	126·4	134	124·9	133·6	129·2	128·3	124·1	129·6	76·9	110·7
Dy	391	1013	988	938	916	933	934	964	925	971	980	928	955	934	643	838
Ho	95·8	222·6	209	204	204	208	206	208	204·4	222	223	218	208	204	157	188
Er	326	667	619	627	618	620	655	628	602	662	677	681	651	625	520	595
Tm	60·5	109·3	99·2	94·8	99·0	100·0	102·0	93·5	97·8	110·9	108·0	113·4	109·0	99·0	94·0	99·7
Yb	444	726	681	668	677	688	708	656	659	735	738	766	713	646	700	638
Lu	48·9	82·1	76·2	74·6	77·5	74·7	79·0	71·0	71·1	80·9	81·7	84·6	79·8	74·4	78·8	72·0
Y	2850	5060	4770	4670	4550	4600	4840	4890	5000	4840	5100	4700	4840	4880	4220	4590
Hf	1032	2580	2380	2520	2630	2170	2610	2180	2060	2530	2270	2580	2520	2310	2450	2400
Nb	3220	8360	7570	6080	6020	7130	8310	5390	5580	7320	8380	6390	7510	6830	5620	6860
Ta	127	975	759	579	601	1000	694	403	390	899	975	573	855	639	847	770
Pb	41·6	87·3	106·0	102·0	90·0	117·7	89·8	43·2	47·1	117·1	151·9	121·2	108·0	54·4	66·4	72·3
Th	27·3	16·7	19·8	18·5	18·7	18·6	20·4	18·3	19·2	18·6	18·9	17·8	19·8	16·3	38·4	40·5
U	30·1	16·1	26·4	24·0	22·0	25·8	30·0	18·8	24·3	25·2	27·9	23·7	24·1	15·5	50·9	20·6

[a]r, rim; c, core; do, BSE-dark overgrowth; bo, BSE-bright overgrowth.
[b]All LA-ICPMS data, including analytical errors and detection limits, are given in Supplementary data II.

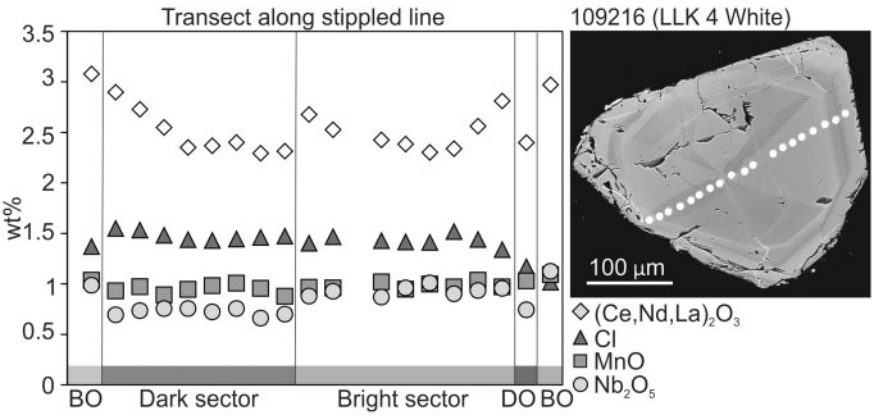

Fig. 6. Compositional variations in REE, Cl, Mn and Nb (wt %) across a sector-zoned EGM grain, analyzed using 5 μm spot size for higher spatial resolution, compromising the quality of Na and Ca results. DO, dark overgrowth, BO, bright overgrowth. Errors are smaller than symbols.

EGM overgrowths

Some EGM cores are overgrown by partial or complete concentric rims with irregular contacts to surrounding phases (Fig. 5a, b). The overgrowths generally lack oscillatory and sector zoning and reveal greater compositional variability than the cores. Multiple overgrowths with variable BSE intensities may be observed on a single EGM crystal (Figs 5 and 6). No systematic patterns, e.g. dark then bright-BSE or *vice versa* were identified.

Dark overgrowths (filled triangles in Fig. 7) are only observed in the LLK sequence and are most abundant in the white kakortokites of the lower LLK where EGM are relatively coarse grained (0·5–4 mm). They exhibit lower REE, Y, Nb, Mn and Hf, but higher Fe compared to the cores (Fig. 7). Conversely, BSE-brighter overgrowths (open triangles, Fig. 7) are enriched in REE + Y and Nb (+0·5 and +0·2 apfu, respectively) relative to cores and are observed mostly on EGM from the upper LLK, TLK and aegirine lujavrite. Variations in REE + Y and Nb between EGM cores and their overgrowths increase upwards and are most pronounced within the TLK (Fig. 7b, c, g). Brighter overgrowths have elevated mean contents of Mn (+0·1 apfu), K (+0·1 apfu) and lower Fe (-0·25 apfu), Al (-0·05 apfu), Na (down to 7 apfu) and Hf (-0·1 apfu) relative to the cores (Table 2). Chlorine contents in the overgrowths are consistently lower than in cores (*c.* -0·5 to 1 apfu, Fig. 7d).

Stratigraphic variations in EGM cores

The EGM cores display a continuous upwards decrease in Ca (6·2–4·8 apfu) and Cl (1·5–1 apfu), and a complementary increase in Mn (0·3–0·6 apfu) and REE + Y (0·4–1 apfu) across the LLK to the TLK (Table 2; Fig. 7). Across the LLK, EGM Fe/Mn ratios vary strongly between black, red and white sublayers, with the most extreme range (13 to 3) seen in unit -4 (Fig. 7a). A marked decrease in Fe/Mn ratios is apparent in the overlying TLK and aegirine lujavrites (from 9 to 3).

Sodium contents are fairly constant at 13–14 apfu in the LLK, decreasing slightly in the aegirine lujavrite. Similarly, K contents are constant in the LLK (0·20–0·15 apfu), but then increase in the upper TLK and lower aegirine lujavrites, reaching 0·4 apfu. The REE + Y increase gradually from 0·4 apfu in the LLK to 0·6 apfu in the lower part of the TLK sequence and sharply increase to 1·0 apfu in the upper TLK and aegirine lujavrite I. In contrast, Hf and Ti decrease upwards from 0·04 to 0·03 apfu and from 0·03 to 0·01 apfu, respectively. Niobium also decreases up the LLK (0·3–0·15 apfu), but shows a reversal in the lujavrites (Fig. 7). EGM from the basal parts of the marginal pegmatite exhibit the highest Cl, Ca, Hf, Nb and Ti contents and the lowest REE + Y and Mn contents of the sequence (Fig. 7).

Selected trace elements

Trace element systematics were studied based on a total of 21 EGM core–rim traverses. Core–rim zonation is most clearly recorded by the large ion lithophile elements (LILE) Ba, Rb and Pb, with EGM from white kakortokites showing the most pronounced trends (Fig. 8). Barium is inversely correlated with Rb and Pb, with Ba increasing significantly from core to rim from ~300 to 1200 ppm, and Pb and Rb decreasing from ~160 to 40 ppm and from 20 to 7 ppm, respectively. EGM cores from layer -4 W have higher average Ba (*c.* 600 ppm) and lower Pb (*c.* 80 ppm) than EGM from the corresponding layer of layer -4B (*c.* 300 ppm Ba and *c.* 250 ppm Pb). Some bright overgrowths are enriched in Ba (*c.* 1400 ppm, Fig. 8) and show simultaneous enrichment in Pb, U and Th (Fig. 9b). As for REE and Nb, dark EGM overgrowths show Ba, Rb and Pb systematics that contrast with general core-rim trends in the sector-zoned cores (Fig. 8).

Uranium and Th are more or less constant across the cores (~30 and 20 ppm, respectively), while some overgrowths are significantly enriched (up to 300 ppm U and 120 ppm Th, Fig. 8). This is associated with an increase in Th/U (~0·6–0·8 in cores, up to 2 in overgrowths). Crystal-scale variations in Ta range between 600 and 1000 ppm and appear to be correlated with sectoral variations in Nb, thus yielding relatively constant Nb/Ta (~7–10) across sector boundaries. Tantalum and Hf

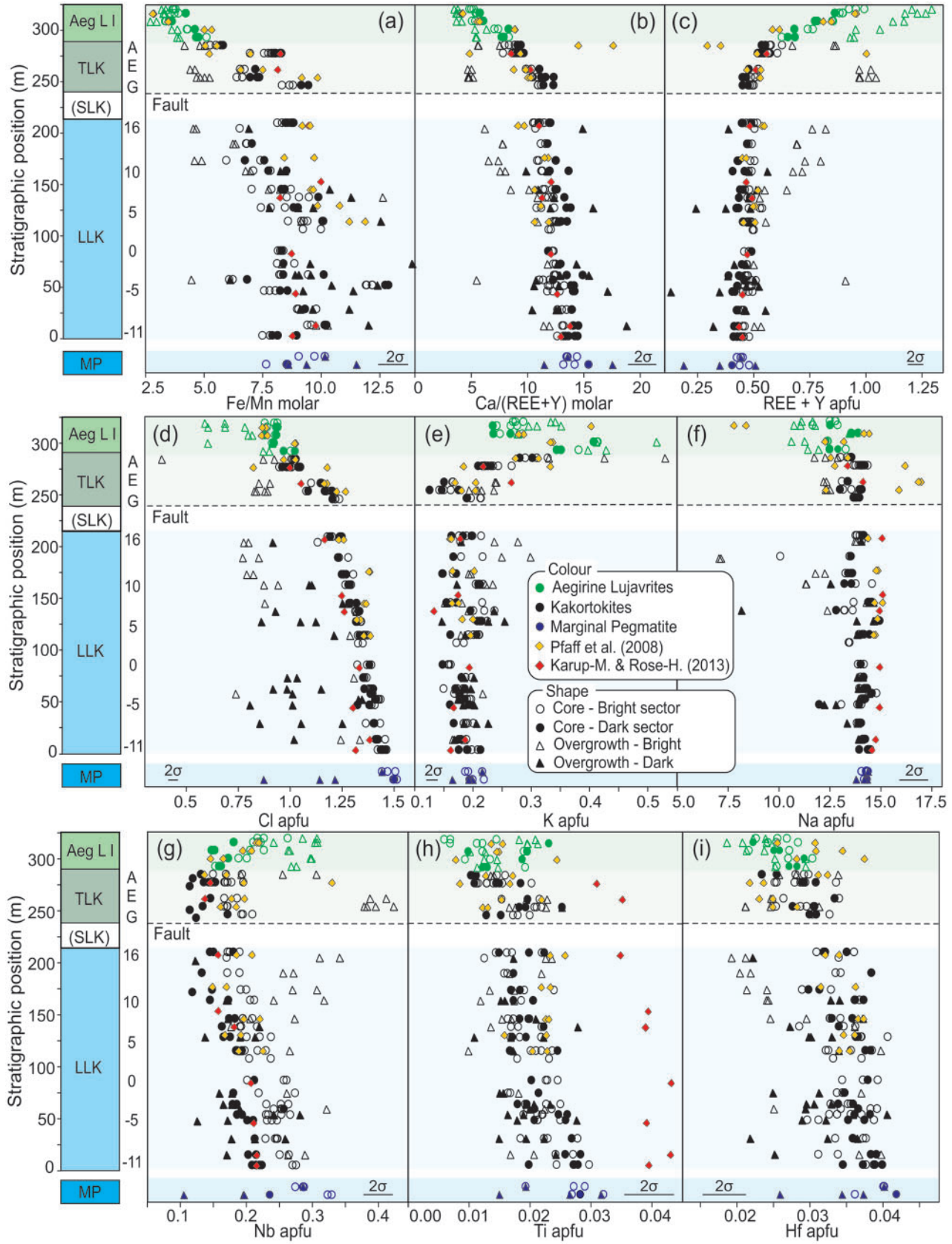

Fig. 7. Compositional variations in (a) Fe/Mn and (b) Ca/(REE+Y) molar ratios, and (d) REE+Y, (d) Cl, (e) K, (f) Na, (g) Nb, (h) Ti and (i) Hf in apfu values for EGM cores and overgrowths plotted against stratigraphy. Literature values (Pfaff *et al.* 2008; Karup-Møller & Rose-Hansen, 2013) shown for comparison. Plotted values are means of individual analyses (n = 1 to 6) per crystallographic segment. Average 2σ of plotted means indicated by scale bars.

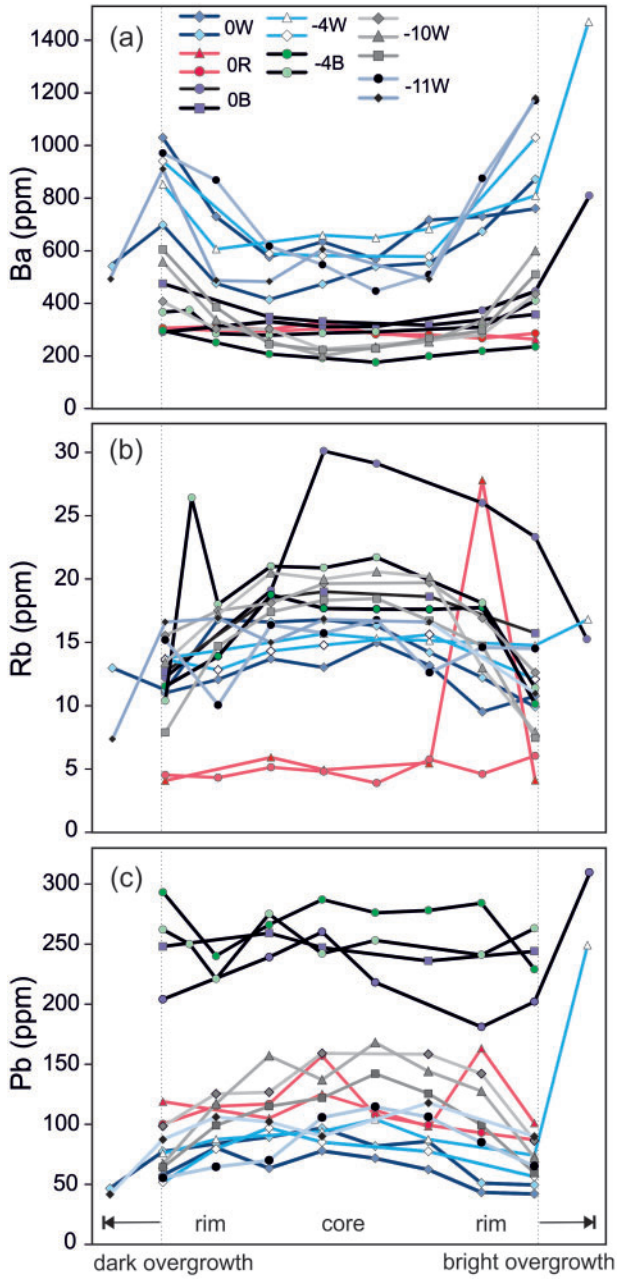

Fig. 8. Core–rim profiles for (a) Ba, (b) Rb and (c) Pb in EGM from the lower LLK. Note rimward enrichment in Ba and complementary depletion in Rb and Pb, particularly in EGM from white kakortokites. The REE–Nb–Hf and U–Th–Pb relations for an EGM grain from layer -4 W (with BSE-bright overgrowth enriched in Ba, Rb and Pb) are shown in Fig. 9.

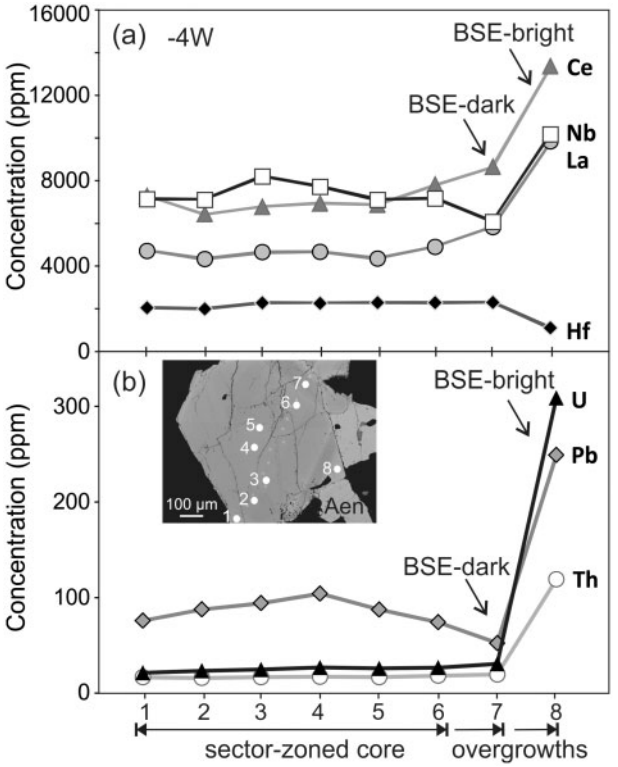

Fig. 9. Trace element core–rim profiles from EGM grain nr. 1 in -4 W (also in Figs 8 and 10a), showing element relations for (a) Ce, La, Nb and Hf and (b) Pb, U and Th. Note rimward increase in Ce and La, lower Nb contents in dark rim and decoupling of Nb from Hf (also Ta, see text) in the bright overgrowth.

may decrease significantly in both bright and dark overgrowths (lowest values 127 ppm Ta and 1000 ppm Hf), and are associated with an increase in Nb/Hf (~3 in cores to 9 in overgrowths) and Nb/Ta (~10 in cores to 25 in overgrowths). The latter exceeds the reported range of Nb/Ta of 10–18 in EGM cores in the kakortokites (Pfaff *et al.*, 2008). Total REE contents are positively correlated with LREE enrichment (e.g. $(La/Yb)_N$, Figs 9 and 10). Within a single grain $(La/Yb)_N$ may increase from 4 to 7, mostly reflecting steepening HREE slopes ($(Gd/Yb)_N$ from 0·8 to 1·2, Fig. 11). Conversely, LREE slopes decrease with increasing REE contents ($(La/Sm)_N$ from 5 to 3·5, Fig. 10). Some dark (REE–Nb poor) EGM overgrowths reveal marked changes in primitive mantle normalized REE patterns and show significant MREE depletion relative to LREE and HREE, yielding high $(La/Sm)_N$ (up to 7) and positive HREE slopes ($(Gd/Yb)_N$ of 0·56). All EGM have negative Eu anomalies between 0·2 and 0·4 (average Eu/Eu* = 0·25), and no systematic core-rim or stratigraphic trends are observed.

DISCUSSION

Previous models on the origin of kakortokite layering

Contrasting models for the origin of the repetitive kakortokite layering at Ilímaussaq have been proposed in recent literature (Pfaff *et al.*, 2008; Lindhuber *et al.*, 2015; Marks & Markl, 2015; Hunt *et al.*, 2017), broadly representing two endmembers. One describes closed system evolution with layering caused by density separation and crystal mat formation (Lindhuber *et al.*, 2015; Marks & Markl, 2015). The other describes an open magmatic system with layering induced by repeated replenishment and nucleation sequences linked to variations in volatile concentrations (Pfaff *et al.*, 2008; Hunt *et al.*, 2017). We first discuss the proposed models in more

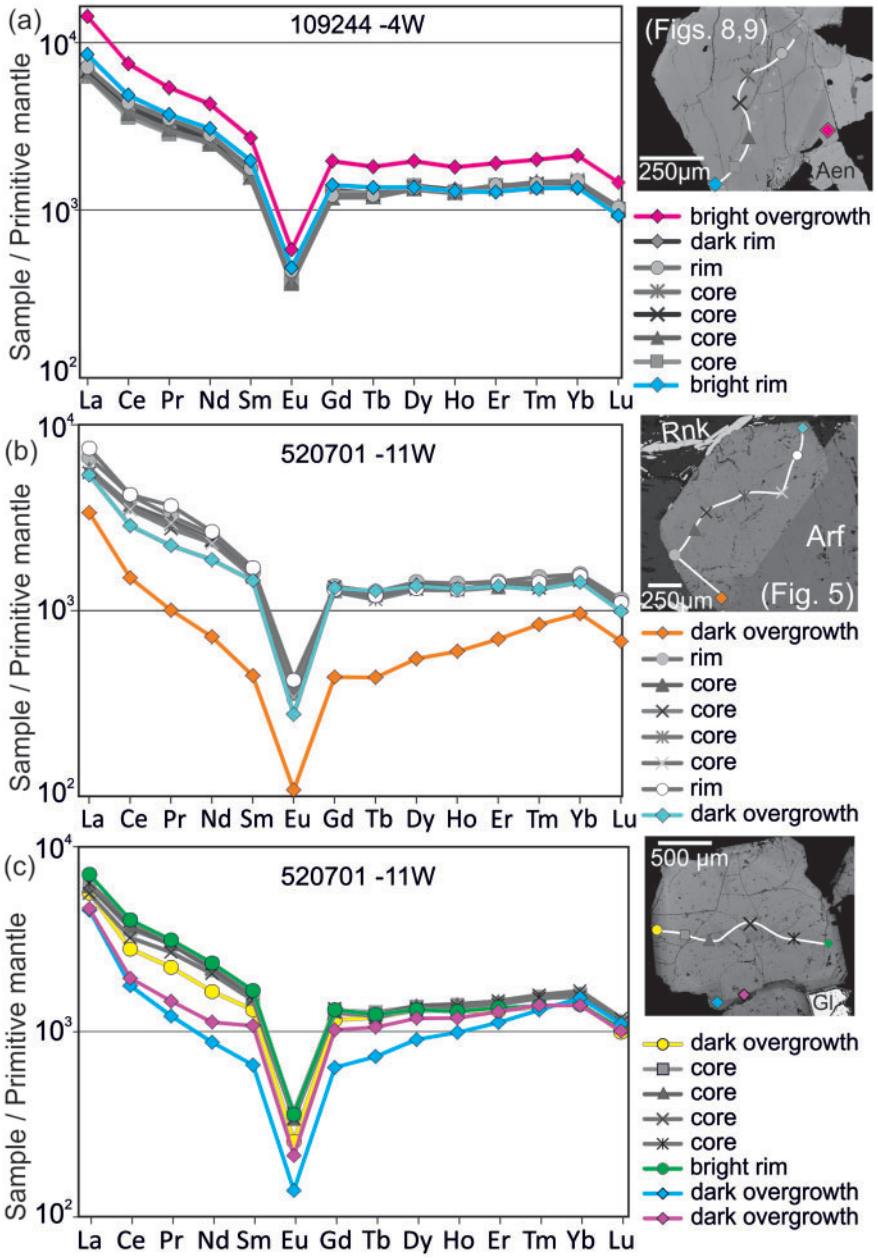

Fig. 10. Primitive mantle normalized (Palme & O'Neill, 2003) REE patterns for selected EGM transects for (a) grain nr. 1 in unit -4 white and (b, c) grain nr. 1 and 3 in unit -11 White, illustrating crystal scale REE variations. See data in Table 3. Gl, galena.

detail below, as these very different models have fundamental implications for how we understand the evolution the agpaitic melts and the kakortokite–lujavrite sequence as a whole, and thus how we interpret our compositional EGM data. In the discussion that follows, we place particular emphasis on bulk and mush melt evolution trends based on the compositional variations in EGM cores and overgrowths.

Closed system: crystal mats

Based on rhythmic trends in the Fe/Mn ratios of EGM and amphiboles between consecutive black, red and white kakortokite layers, Lindhuber *et al.*, (2015) proposed crystal mat formation as a layering mechanism for the kakortokites. This process was originally described by Lauder (1964), and numerically simulated ('traffic jam' model) by Bons *et al.* (2014). A comparable model, referred to as 'self-stratification' was described by Nielsen & Bernstein (2009) and further developed by Nielsen *et al.* (2015) to explain the formation of plagioclase and pyroxene macrolayers in the Skaergaard intrusion.

The model describes the formation of semi-impermeable 'mats' through crowding effects between phases with differential settling velocities. In the kakortokites, following Lindhuber *et al.* (2015), amphibole, EGM, nepheline and alkali feldspar nucleated more or

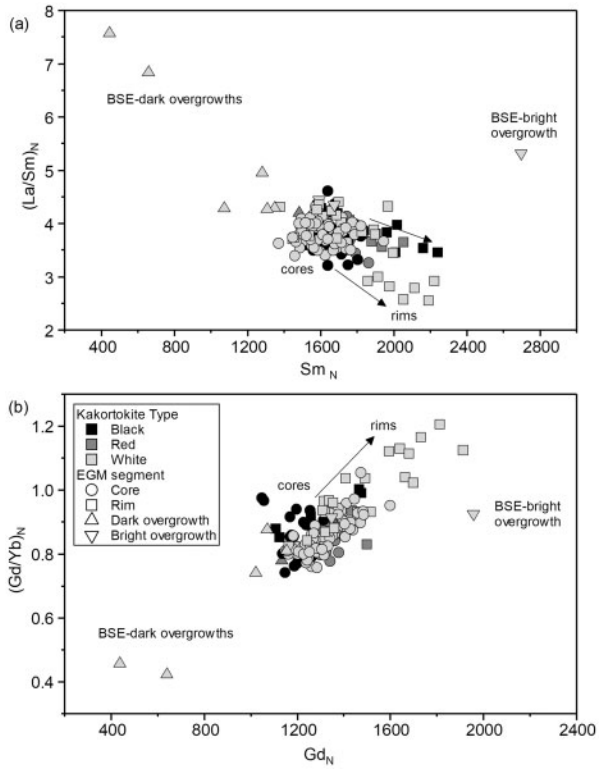

Fig. 11. Rare earth element fractionation patterns from core-rim for LA-ICP-MS data of EGM (a) LREE fractionation plot illustrating progressive decrease in $(La/Sm)_N$ ratios with increasing REE contents from core to rim. Higher $(La/Sm)_N$ ratios in EGM overgrowths could reflect fractionation of rinkite with low $(La/Sm)_N$. (b) HREE fractionation plot showing positive correlation between $(Gd/Yb)_N$ ratios and Gd_N, i.e. increasing HREE slopes with increasing REE contents. Normalized to primitive mantle (Palme & O'Neill, 2003).

less contemporaneously throughout the magma chamber to explain the absence of (recorded) EGM fractionation trends across the series (Pfaff *et al.*, 2008). Amphibole sank faster than EGM, nepheline and feldspar (the latter may even have been buoyant) and aggregated at certain levels to form mats that progressively hindered physical and chemical exchange between the underlying and overlying crystal mushes, thus creating 'quasi-independent crystallization cells' (Lindhuber *et al.*, 2015; Marks and Markl, 2015). Continued density separation of amphibole, EGM, nepheline and alkali feldspar between two mats led to the characteristic tripartite modal layering. Differentiation of the isolated melt between two mats accounts for the sequential decrease in EGM Fe/Mn ratios upwards through a tripartite unit, i.e. EGM in black kakortokites crystallized from the bulk melt, while those in the red and white layers crystallized from the progressively more fractionated melts in between (Lindhuber *et al.*, 2015).

Although this model elegantly explains the rhythmicity of the layering, as well the absence of strong fractional crystallization trends across the layered sequence, by sequentially isolating sub-volumes of melt, its feasibility is still questioned. Arguments against it include the absence of a naujaite-like sodalite-rich top layer, the absence of sag or melt escape features and textural studies of unit 0 black indicating *in situ* growth rather than settling as a dominant mode of crystallization (Hunt *et al.*, 2017).

Open system: nucleation sequences through replenishment

Various authors have speculated that the kakortokite layering resulted from repeated replenishment of the magma chamber (Pfaff *et al.*, 2008; Hunt *et al.*, 2017). Most recently, Hunt *et al.* (2017) explored different modes of crystal development across unit 0 using detailed crystal size distribution studies (CSD). Their data suggested that *in situ* crystallization of amphibole and EGM, not settling, dominated during formation of layers 0B and 0R, respectively. This was explained by a nucleation sequence of first amphibole and then EGM, both triggered by the influx of an aphyric melt ponding on the chamber floor. Being more primitive and enriched in Fe, this melt was denser than the resident magma and supersaturated in all mineral phases, but high volatile contents initially inhibited nucleation. As the basal magma cooled, arfvedsonite was the first mineral to nucleate at the mush–magma interface. Continued *in situ* arfvedsonite growth and upward loss of volatiles caused a decrease in halogen contents and triggered nucleation of EGM. Further thermal and chemical equilibration with the resident magma then allowed for all phases to crystallize simultaneously and form layer 0W. Although the model was primarily developed for unit 0, a nucleation cycle induced by replenishment was inferred as potential layering mechanism for the entire sequence. Similar mechanisms of volatile-controlled nucleation sequences were invoked by Pfaff *et al.* (2008) and Larsen & Sørensen (1987). The latter authors, however, envisaged that this occurred through double diffusive loss of heat and volatiles in a compositionally stratified magma chamber rather than through melt influx.

Occasional replenishment of the kakortokite melt can certainly not be discounted, and the role of sequential nucleation of liquidus phases also merits further investigation. However, we find several observations are inconsistent with a periodic replenishment model for the entire sequence. Firstly, our data demonstrate complete compositional continuity of EGM stratigraphically up through the kakortokites (Fig. 7). This is difficult to reconcile with periodic replenishment and would require that the incoming melts fractionated identical agpaitic mineral assemblages in an underlying unexposed magma chamber. Moreover, the striking upward decrease in Cl in EGM across the sequence (Fig. 7d) is inconsistent with sequential changes in volatile contents as the driving force for nucleation, and instead suggests that Cl was gradually depleted from the melt. We expect that influxes of aphyric melts ponding on the white

kakortokite mush would lead to features indicative of physical disturbance and reworking of the cumulate pile. With the exception of the hybrid kakortokites, recently suggested to represent mixing of kakortokite mush with more primitive Ti-rich melts (Hunt, 2015), such features are rare or absent, particularly in the center of the intrusion. A dense basal melt would be expected to fill topographic lows in the chamber floor and thus produce variations in the thickness of the layer around and above autholiths, and towards the margins. Instead, the layers are conspicuously uniform along strike and around autoliths. All in all, a regularly episodic influx of similar volumes of melt, themselves constantly changing composition, would be necessary to account for the regularity of the layering, their relatively constant thickness and the geochemical continuity reported here. This requires a very specific set of unusual circumstances, which in our opinion makes a replenishment model unlikely. Instead, we infer that a closed-system evolution model with internally controlled, self-regulating crystallization processes is more likely to explain the layering (c.f. Larsen & Sørensen, 1987; Sørensen & Larsen, 1987; Bons *et al.*, 2014; Lindhuber *et al.*, 2015).

Bulk melt evolution inferred from EGM core compositions

The subtle upward fractionation trends recorded in the cores of EGM across the kakortokite series, including decreasing Ca, Ti, Nb and Cl and increasing Mn, REE and Y (Fig. 7) are consistent with a continuous closed system evolution model for the kakortokites. All trends are coherent with previously identified trends in EGM from the overlying lujavrites, where compositional changes are more pronounced (Pfaff *et al.*, 2008; Ratschbacher *et al.*, 2015), suggesting similar processes operated throughout. Our data now extends these trends into the previously underexplored lower half of the kakortokite sequence (unit -11 to 0). The most prominent feature is the upward decrease in Cl, from 1·5 apfu in the lowermost LLK and marginal pegmatite to 1·2 apfu in unit +16. This declines to 1 apfu in the aegirine lujavrites I, and eventually reaches 0·5 apfu in the arfvedsonite lujavrite (Ratschbacher *et al.*, 2015). Eudialyte thus monitors a progressive depletion of Cl in the melt, which is likely coupled to a progressive enrichment in H_2O, and caused by the voluminous crystallization of Cl-rich EGM and sodalite (Pfaff *et al.*, 2008; Ratschbacher *et al.*, 2015).

In previous studies, the absence of upward mineral fractionation trends across the LLK, notably in Fe/Mn and Ca/(REE + Y) ratios, was poorly understood and led to unnecessary complexity in the proposed crystallization models. For example, Pfaff *et al.* (2008) argued for repeated replenishment with similar composition melts, such that fractionation trends would not be visible. Lindhuber *et al.* (2015) explained the absence of fractionation trends in EGM from consecutive black layers by contemporaneous nucleation of early cumulus phases and simultaneous development of crystal mats throughout the entire magma column. However, the upward trends in Ca/(REE + Y), Nb, Ti and Cl, and to a minor extent in Fe/Mn identified here (Fig. 7), indicate that the kakortokites gradually crystallized upwards from the floor (c.f. Ferguson, 1970; Larsen & Sørensen, 1987).

We infer that the compositional trends in the EGM cores, i.e. stratigraphic (this study) and superimposed rhythmic trends in Fe/Mn (Lindhuber *et al.*, 2015), as well as evidence for *in situ* crystallization (Hunt *et al.*, 2017), are all consistent with a somewhat adjusted interpretation of mat formation, hereafter referred to as 'compartmentalization'.

In this model, the kakortokite proto-units formed through self-organization in an upward migrating crystallization front through combined processes of nucleation, *in situ* growth, gravitational separation and loss of residual melt and volatiles. These units would develop into isolated mush compartments in which internal melt fractionation and density segregation led to the striking modal layering and Fe/Mn variations. Each proto-black layer developed at the nucleation front initially consisted of small amphibole nuclei, which subsequently grew *in situ.* Amphiboles and other liquidus phases nucleated at the crystallization front, but only amphiboles would be preserved, as feldspathoids and feldspar nuclei formed at the same front would rise up into the bulk liquid and subsequently may be re-dissolved in hotter regimes. Below the crystallization front, rising feldspars and feldspathoids were trapped below a developing black layer and contributed to the development of the mush compartments as described by mat formation (c.f. Bons *et al.*, 2014; Lindhuber *et al.*, 2015)

Upward loss of residual melts and volatiles from the mush compartments to overlying compartments, and eventually to the bulk melt, would allow for compaction and subsequent draping of layers over sunken roof blocks. The returned mush melts, in turn, contributed to the overall chemical evolution of the bulk melt. The upward fractionation trends of the EGM cores are so gradual (Fig. 7) that they are consistent with a few compartments developing at the same time, but the overall sequence of nucleation, density separation, compartmentalization, and *in situ* growth must have progressed systematically upwards. This is consistent with views of cumulate formation and layering in inward-migrating solidification fronts or 'mushy boundary layers' in cooling magma chambers (e.g. Marsh, 1995; Namur *et al.*, 2015; Nielsen *et al.*, 2015). Differentiation of the bulk kakortokite melt as such can be visualized as the net result of *in situ* crystallization (c.f. Langmuir, 1989) and the return of residual melts and components not trapped in crystallizing phases and interstitial melt pockets within the kakortokite compartments. Hence, key information lies within the chemical evolution of the mush melts between two consecutive black layers, explored from EGM overgrowths compositions below.

Mush melt evolution inferred from EGM overgrowths

Compositions of EGM overgrowths diverge significantly from the EGM cores. These suggest major changes in melt chemistry and connectivity and may mark the transition between open system crystallization (e.g. euhedral sector-zoned cores) to crystallization from isolated intercumulus -or mush- melts (e.g. irregular overgrowths). Here, we hypothesize that contrasting evolution for EGM overgrowths, either with low Nb–REE–Y (BSE-dark) or high Nb–REE–Y contents (BSE-bright) relative to the overall fractionation trends recorded in the cores, reflect changing co-crystallizing phase assemblages at the intercumulus stage. High REE + Y, coupled with lower Hf, Al and Fe/Mn in the BSE-bright overgrowths, are in accordance with upward bulk melt fractionation trends recorded in the cores. The coupled increase in Nb with increasing REE + Y in the same overgrowths, however, is inconsistent with upward decrease in Nb in the cores (Fig. 7). By contrast, BSE-dark overgrowths are more 'primitive' in terms of Ca/(REE + Y), Fe/Mn and REE patterns, while the lower Hf, Ti, Nb and Cl contents are consistent with overall bulk melt fractionation trends.

Dark EGM overgrowths are most abundant in the lower section of the LLK. In this part of the sequence, late-magmatic rinkite is a common intercumulus phase. Rinkite contains approximately 20 wt % $LREE_2O_3$, 3–6 wt % Nb_2O_5 and 5–7 wt % TiO_2 (Rønsbo *et al.*, 2014), and thus represents an important host for REE and Nb. In the overlying TLK and aegirine lujavrite I (Fig. 7) BSE-dark EGM overgrowths are essentially absent, and this is coupled with an absence of rinkite as an interstitial phase. Rinkite crystallization would effectively sequester F, Ca and HFSE from the mush melt, and its timing of crystallization may thus be recorded by a sudden drop in Nb–REE–Y in EGM overgrowths.

Rinkite crystallization requires high F, REE and Ti concentrations in the melt, as well as overall high peralkalinity (e.g. Andersen & Friis, 2015). Assuming F and REE contents increase with peralkalinity during magmatic evolution, the disappearance of rinkite may reflect the sequential depletion in Ti (as well as Nb and Ca) in the melt. This is consistent with upwardly decreasing Ti in both whole-rock (e.g. Bailey *et al.*, 2001) and EGM (this study) compositions, as well as rinkite solid solution trends towards nacareniobsite-(Ce) (Rønsbo *et al.*, 2014; our unpublished data). Progressive Ti depletion may additionally be expressed by the distribution of aenigmatite, which is abundant in the lowermost LLK and underlying, unexposed nepheline syenites (Schønwandt *et al.*, 2016), rare in the upper LLK, and virtually absent in the TLK and aegirine lujavrites (Larsen, 1977). In the absence of intercumulus saturation of rinkite, EGM form the only sink for Nb and REE. As long as sufficient Zr is available for adcumulus EGM growth, overgrowths will record the progressive REE enrichment in the mush melts. The disappearance of rinkite could furthermore explain the reversal towards higher Nb contents in both EGM cores and overgrowths in aegirine lujavrite I (Fig. 5a), if only the combined fractionation of rinkite and EGM was sufficient to deplete the melt in Nb (c.f. Ferguson, 1970).

Alternatively, the shift towards increasing Nb contents in EGM cores and overgrowths in the lujavrites may result from coupled substitution mechanisms in solid solution between eudialyte$_{ss}$ and kentbrooksite (Table 1). With increasing REE and Mn relative to Ca and Fe, respectively (i.e. kentbrooksite), the EGM structure becomes less centrosymmetric and Nb is incorporated more easily (Johnsen & Gault, 1997; Johnsen *et al.*, 2003). The implication would be that Nb partition coefficients in EGM increase during progressive enrichment in REE and Mn, and Nb contents in EGM increase even though Nb is depleted in the coexisting melt. However, this mechanism does not seem to operate in the kakortokites where higher Mn and REE contents do not necessarily correlate with higher Nb.

All EGM overgrowths show a significant decrease in Cl contents, consistent with the progressive depletion in Cl relative to H_2O in the evolving bulk and mush melts. Low Na contents in some EGM overgrowths also fit with this, as hydrogen groups compete with Cl on the X-site (as OH^-) and Na (as H_3O^+) on the N-site (aqualite component; Pfaff *et al.*, 2008). Increasing H_2O activities in the bulk and mush melts are consistent with a near-continuous evolution from agpaitic silicate melt towards aqueous fluids (e.g. Khomyakov, 1995; Müller-Lorch *et al.*, 2007; Markl & Baumgartner, 2002), as is inferred for example from the presence of interstitial analcime and extensive autometasomatic replacement of primary phases by catapleiite, analcime and natrolite (e.g. Müller-Lorch *et al.*, 2007; Karup-Møller *et al.*, 2010; Borst *et al.*, 2016).

It should be noted that the overgrowths represent a significant volume of EGM, as a crystal with a diameter of 1 mm will increase in volume by 33% with addition of a 0·05 mm concentric rim (10% increase in diameter). In the kakortokites and lujavrites, thicknesses of EGM overgrowths typically range between 5 and 15% of the original crystal radius and the proportion of intercumulus growth thus constitutes between 10 and 50% of the total EGM volume. The implications being: (1) EGM core compositions are not representative for bulk EGM in a given rock, and (2) *in situ* crystallization and fractionation of mush melts play an important role in the evolution of the kakortokites and lujavrites.

Insights from EGM trace element zonation

Compositional core–rim trends in the sector-zoned EGM cores as well as overgrowths are particularly evident for the LILE group (Ba, Rb, Pb; Fig. 8). These trends may reflect changes in the proportions of these elements in the evolving bulk and mush melt or in LILE partitioning behavior between melt, EGM and co-crystallizing phases, and, therefore, could provide insights into relative timings of crystallization and density separation with respect to compartmentalization.

The rimward decrease in Pb in EGM of the white kakortokites, for example, may reflect a progressive Pb depletion by crystallization of accessory galena, which is more abundant in white than in black and red kakortokite (Karup-Møller, 1978). Barium, which is negatively correlated with Pb and Rb (Fig. 8), mostly occupies the N-site which can also incorporate significant Sr (taseqite endmember, Petersen *et al.*, 2004). Lead and Rb are generally less compatible in EGM than Sr and Ba, and have no particular site preference. The dominant host for Rb is alkali feldspar, reflected in high Rb contents (600 ppm) in white kakortokites and positive correlations with whole-rock Al, Si and K (Bailey *et al.*, 2001). Whole-rock Ba budgets are controlled by EGM, reflected by maximum whole-rock Ba contents in red kakortokites (>1000 ppm) and positive correlations with Zr and Ca (Bailey *et al.*, 2001). Whole-rock, amphibole, EGM, and alkali feldspar Rb contents gently increase with magmatic evolution (Bailey *et al.*, 2001; Pfaff *et al.*, 2008), suggesting relative Rb enrichment despite voluminous crystallization of alkali feldspar. The rimward decrease in Rb in EGM (Fig. 8) thus stands in contrast with overall bulk melt evolution. Barium whole-rock contents gently decrease upward through the kakortokites (Bailey *et al.*, 2001), suggesting that Ba was gradually depleted by fractionation of EGM (c. 200 – 1400 ppm) and alkali feldspar (c. 300 ppm, unpublished data). If those trends are real, both the rimward decrease in Rb and increase in Ba in EGM contrast with overall Rb and Ba fractionation trends, and instead, may reflect changing LILE partitioning with increasing volatile contents in the mush melts. Importantly, however, the fact that these trends are also observed on a rhythmic scale between black, red and white layers is consistent with fractionation in compartmentalized macrolayers, where EGM cores and overgrowths in white kakortokites crystallized from more fractionated bulk and mush melts, respectively, assembled in the upper parts of the compartments. A wider set of more closely spaced samples, in conjunction with trace element analyses of co-crystallizing minerals, would be needed to verify this.

High U and Th in some of the bright EGM overgrowths (Fig. 9), particularly in white kakortokites, mark the progressive U–Th enrichment in the mush melts, consistent with the overall increase in U of the bulk melt as recorded in EGM across the kakortokite-lujavrite sequence (Steenfelt & Bohse, 1975; Bailey *et al.*, 2001; Pfaff *et al.*, 2008) and culminating in the stabilization of steenstrupine-(Ce) at the expense of EGM in the hyperagpaitic lujavrites (e.g. Sørensen & Larsen, 2001; Sørensen *et al.*, 2011). As EGM have lower Th/U (*c.* 0·3–0·8) than the inferred parental agpaitic melts (*c.* 3, Bailey *et al.*, 2001), Th/U ratios tend to increase with U–Th enrichment. This is well recorded by EGM overgrowths, most clearly in those of white kakortokites (Th/U of up to 2).

Primitive-mantle normalized REE patterns from EGM core-rim transects reveal decreasing LREE slopes (i.e. $(La/Sm)_N$) and increasing HREE slopes ($(Gd/Lu)_N$) with increasing total REE towards the rims (Fig. 11). Pfaff *et al.* (2008) reported similar trends, i.e. increasing $(Gd/Lu)_N$ ratios and decreasing $(La/Sm)_N$ up sequence. Hence, core-rim trends in individual grains and up section average core trends are consistent with bulk melt fractionation as recorded by increasing whole-rock LREE/HREE (Bailey *et al.*, 2001). The overgrowths, however, show contrasting LREE/HREE fractionation patterns and can thus be considered more 'primitive' in their REE signature (Fig. 11). Reported REE concentrations (La, Ce, Pr, Nd, Sm and Y) in rinkite (Rønsbo *et al.*, 2014) exceed the normalized REE patterns of EGM by *c.* one order of magnitude and show distinctly positive Ce anomalies coupled with low La/Sm_N ratios relative to EGM. Hence, intercumulus rinkite fractionation could be a plausible mechanism to explain the relative Ce depletion and increasing La/Sm_N ratios in the mush melts, subsequently recorded by more 'primitive' LREE patterns in some EGM overgrowths (Figs 10c, 11).

Kakortokite–lujavrite transition and the origin of the Lakseelv fault zone

The TLK were traditionally interpreted to stratigraphically overly the LLK, now juxtaposed by a northern downthrow along the Lakseelv hinge-fault (e.g. Bohse *et al.*, 1971; Bohse & Andersen, 1981; Larsen & Sørensen, 1987). Based on textural and structural observations Ratschbacher *et al.* (2015) suggested a model in which the TLK and aegirine lujavrites in the Lakseelv area were emplaced as a separate sill structure that intruded the LLK and naujaites along a steep feeder zone, thereby challenging the traditional view of continuous evolution for the kakortokite–lujavrite sequence.

The uninterrupted trends in EGM compositions on either side of the Lakseelv fault (Fig. 7) require that the TLK-lujavrite forming melt was identical to that of the residual bulk kakortokite melt. Such a model again requires an underlying magma reservoir that has undergone an identical crystallization sequence to that displayed in the kakortokites. Although we find such a scenario unlikely, a separate intrusive history for the LLK and TLK-lujavrite cannot be excluded, particularly in the absence of compositional data for the SLK which represent the only immediate link between the LLK and TLK on either side of the fault.

Alternatively, the deformation textures observed in the Lakseelv fault zone (Ratschbacher *et al*, 2015) may be explained by large scale disruption of the magma chamber at near- and sub-solidus conditions for the upper TLK and aegirine lujavrites (i.e. foliation, Fig. 4f) and sub-solidus conditions for the lower TLK (i.e. brittle deformation, Fig. 4e). Syn-magmatic fault movement triggered by roof collapse and, or, reactivation of pre-existing fault structures in the basement could lead to the injection of crystal rich kakortokite–lujavrite mushes into structural zones of weakness. This would halt the

effectiveness of compartmentalization, as quiescent conditions are no longer met. The redistribution of mushes would resemble a sill structure as described by Ratschbacher *et al.* (2015), but does not require the influx of a new melt. Examples in which replenishment of the Ilímaussaq magma chamber is argued for, e.g. in the more evolved arfvedsonite and medium-coarse grained lujavrites (e.g. Sørensen *et al.*, 2006*a*, 2006*b*; Ratschbacher *et al.*, 2015), as well as in the 'hybrid' kakortokites in the lower part of the complex (Hunt, 2015), have all been supported by observable jumps in mineral chemistry, intrusive contacts or other dynamic features, but they do not rule out dynamic redistributions of melts and mushes within the magma chamber. In summary, we find that the upward differentiation trends recorded in EGM cores and rims across the LLK, TLK and aegirine lujavrite sequence are consistent with a closed system evolution model following upward compartmentalization of a single agpaitic melt at the floor of the magma chamber.

CONCLUSIONS

This work describes magmatic fractionation trends in complexly zoned eudialyte-group minerals from the kakortokite–lujavrite sequence of the Ilímaussaq complex. Sector-zoned cores and concentric overgrowths are interpreted to record bulk and mush melt evolution trends, respectively. The sector-zoning is associated with minor variations in Nb, REE and Y and reflects differential HFSE partitioning on non-equivalent crystal faces. Average compositions for the sector-zoned EGM cores reveal a gradual upward decrease in Ca/(REE + Y), Fe/Mn, Ti, Nb and Cl contents through the lower layered kakortokites, which continue and intensify in the overlying transitional kakortokites and aegirine lujavrites. We interpret these data to monitor the continuous differentiation of a single agpaitic bulk melt. Layering developed through repeated processes of nucleation and density separation within an upward migrating crystallization front. We propose a model where layering occurred through progressive compartmentalization of the kakortokite mush, initially by gravitational separation along the lines of mat formation (c.f. Bons *et al.* 2014; Lindhuber *et al.*, 2015). However, the model differs from mat formation in that crystallization progressed systematically upwards and nucleation and *in situ* growth play an integral role. Chemical evolution of the bulk melt by fractional crystallization would be minimal due to the sequential isolation of sub-volumes of melt into kakortokite mush compartments. The fractionation trends in EGM reported here resulted primarily from *in situ* crystallization within the crystallization front (Langmuir, 1989) and differential loss of mush liquids that escaped the crystallization front.

Subhedral EGM overgrowths show a compositional variability that exceeds overall stratigraphic changes recorded in the EGM cores, resulting from more efficient fractionation of mush melts by *in situ* crystallization, locally following differentiation paths that are different from the contemporaneous bulk melt. The overgrowths also reveal systematic compositional changes across the stratigraphy, which we infer to reflect the onset and, or, disappearance of co-crystallizing intercumulus phases such as rinkite and aenigmatite, as well as changing layering dynamics (decreasing efficiency of compartmentalization) between the lower layered kakortokites, the transitional kakortokites and the aegirine lujavrites due to diminished melt volumes and physical disruption.

Trace element systematics (e.g. Ba, Rb, Pb, U, Th) in EGM from the kakortokites lend further support to a compartmentalized crystallization model, with EGM in white kakortokites showing the most prominent zoning patterns suggesting they crystallized from more evolved mush melts in the upper parts of the compartments. Finally, we infer that continuous EGM compositions across the kakortokite–lujavrite transition suggest a direct genetic relationship between the kakortokites south and north of the Lakseelv fault. Textural and structural observations in the transitional kakortokites and aegirine lujavrites of the Lakseelv area (i.e. foliation and microfracturing) may be explained by syn- and post-magmatic movement along the Lakseelv fault zone during roof collapse and structural reconfiguration of the magma chamber in the final stages of consolidation.

ACKNOWLEDGEMENTS

This study is published with permission of the Geological Survey of Denmark and Greenland. We thank Muriel Erambert, Matthijs Smit, Tonny Bernt Thomsen and Michael Nielsen for assistance with analyses and sample preparation. Henning Bohse, Per Kalvig and Rune Hende are thanked for geological and logistical support in Greenland. We thank TANBREEZ A/S for providing access to their license area. John Bailey provided samples and constructive comments to an earlier version of the manuscript. We thank Adrian Finch for valuable discussions, and Tom Andersen and Michael Marks for constructive reviews of the manuscript.

FUNDING

This work was financially supported by the Geocenter Denmark under the GreenCrimi project [grant no. 4-2012 Phd-2 to AMB].

SUPPLEMENTARY DATA

Supplementary data are available at *Journal of Petrology* online.

REFERENCES

Andersen, S., Bohse, H. & Steenfelt, A. (1981). A geological section through the southern part of the Ilímaussaq intrusion. *Rapport Grønlands Geologiske Undersøgelse* **103**, 39–42.

Andersen, T. & Friis, H. (2015). The transition from agpaitic to hyperagpaitic magmatic crystallization in the Ilímaussaq alkaline complex, South Greenland. *Journal of Petrology* **56**, 1343–1364.

Andersen, T. & Sørensen, H. (2005). Stability of naujakasite in hyperagpaitic melts and the petrology of naujakasite lujavrite in the Ilímaussaq alkaline complex, South Greenland. *Mineralogical Magazine* **69**, 125–136.

Andersen, T., Erambert, M., Larsen, A. O. & Selbekk, R. S. (2010). Petrology of nepheline syenite pegmatites in the Oslo Rift, Norway: zirconium silicate mineral assemblages as indicators of alkalinity and volatile fugacity in mildly agpaitic magma. *Journal of Petrology* **51**, 2303–2325.

Atanasova, P., Krause, J., Möckel, R., Osbahr, I. & Gutzmer, J. (2015). Electron probe microanalysis of REE in eudialyte group minerals: challenges and solutions. *Microscopy and Microanalysis* **21**, 1096–1113.

Bailey, J. C. (1995). Cryptorhythmic and macrorhythmic layering in aegirine lujavrite, Ilímaussaq alkaline intrusion, South Greenland. *Bulletin of the Geological Society of Denmark* **42**, 1–16.

Bailey, J. C., Gwodz, R., Rose-Hansen, J. & Sørensen, H. (2001). Geochemical overview of the Ilímaussaq alkaline complex, South Greenland. *Geology of Greenland Survey Bulletin* **190**, 35–53.

Bailey, J. C., Sørensen, H., Andersen, T., Kogarko, L. N. & Rose-Hansen, J. (2006). On the origin of microrhythmic layering in arfvedsonite lujavrite from the Ilímaussaq alkaline complex, South Greenland. *Lithos* **91**, 301–318.

Bohse, H. & Andersen, S. (1981). Review of the stratigraphic divisions of the kakortokite and lujavrite in southern Ilímaussaq. *Rapport Grønlands Geologisk Undersøgelse* **103**, 53–62.

Bohse, H., Brooks, C. K. & Kunzendorf, H. (1971). Field observations on the kakortokites of the Ilímaussaq intrusion, South Greenland, including mapping and analyses by portable X-ray fluorescence equipment for zirconium and niobium. *Rapport Grønlands Geologiske Undersøgelse* **38**, 1–43.

Bons, P. D., Baur, A., Elburg, M. A., Lindhuber, M. J., Marks, M. A. W., Soesoo, A., van Milligen, B. P. & Walte, N. P. (2014). Layered intrusions and traffic jams. *Geology* **43**, 71–74.

Borst, A. M., Friis, H., Andersen, T., Waight, T. E., Nielsen, T. F. D. & Smit, M. (2016). Zirconosilicates in the kakortokites of the Ilímaussaq complex, South Greenland: implications for fluid evolution and HFSE-REE mineralization in agpaitic systems. *Mineralogical Magazine* **80**, 1–26.

Cawthorn, R.G. (ed.) (1996). *Layered Intrusions*. Amsterdam: Elsevier.

Cawthorn, R. G., Barnes, S. J., Ballhaus, C. & Malitch, K. N. (2005). Platinum group elements, chromium, and vanadium deposits in mafic and ultramafic rocks. *Economic Geology* **100**, 215–249.

Chakhmouradian, A. R. & Zaitsev, A. N. (2012). Rare earth mineralization in igneous rocks: sources and processes. *Elements* **8**, 347–354.

Charlier, B., Namur, O., Latypov, R. & Tegner, C. (eds) (2015). *Layered Intrusions*. Dordrecht: Springer.

Dowty, E. (1976). Crystal structure and crystal growth: II. Sector zoning in minerals. *American Mineralogist* **61**, 460–469.

Ferguson, J. (1964). Geology of the Ilímaussaq alkaline intrusion, South Greenland. Part 1. Description of map and structure. *Meddelelser om Grønland* **172**, 1–81.

Ferguson, J. (1970). The significance of the kakortokite in the evolution of the Ilímaussaq intrusion, South Greenland. *Bulletin Grønlands Geologiske Undersøgelse* **83**, 1–193.

Garde, A. A., Hamilton, M. A., Chadwick, B., Grocott, J. & McCaffrey, K. J. W. (2002). The Ketilidian orogen of South Greenland: geochronology, tectonics, magmatism, and fore-arc accretion during Palaeoproterozoic oblique convergence. *Canadian Journal of Earth Sciences* **39**, 765–793.

Hunt, E. J. (2015). Magma chamber dynamics in the peralkaline magmas of the Kakortokite Series, South Greenland. Unpublished Ph.D. thesis, University of St Andrews, University of St Andrews, Scotland, pp. 1–230.

Hunt, E. J., Finch, A. A. & Donaldson, C. H. (2017). Layering in peralkaline magmas, Ilímaussaq Complex, S Greenland. *Lithos* **268–271**, 1–15.

International Mineralogical Association (2016). The new IMA list of minerals—a work in progress. http://nrmima.nrm.se//IMA_Master_List_2016_07.pdf.

Johnsen, O. & Gault, R. A. (1997). Chemical variation in eudialyte. *Neues Jahrbuch fur Mineralogie Abhandlungen* **171**, 215–237.

Johnsen, O. & Grice, J. D. (1999). The crystal chemistry of the eudialyte group. *Canadian Mineralogist* **37**, 865–891.

Johnsen, O., Ferraris, G., Gault, R. A., Grice, J. D., Kampf, A. R. & Pekov, I. V. (2003). The nomenclature of eudialyte-group minerals. *Canadian Mineralogist* **41**, 785–794.

Karup-Møller, S. (1978). The ore minerals of the Ilímaussaq intrusion: their mode of occurrence and their conditions of formation. *Bulletin Grønlands Geologisk Undersøgelse* **127**, 51.

Karup-Møller, S. & Rose-Hansen, J. (2013). New data on eudialyte decomposition minerals from kakortokites and associated pegmatites of the Ilímaussaq complex, South Greenland. *Bulletin of the Geological Society of Denmark* **61**, 47–70.

Karup-Møller, S., Rose-Hansen, J. & Sørensen, H. (2010). Eudialyte decomposition minerals with new hitherto undescribed phases from the Ilímaussaq complex, South Greenland. *Bulletin of the Geological Society of Denmark* **58**, 75–88.

Khomyakov, A. P. (1995). *Mineralogy of Hyperagpaitic Alkaline Rocks*. Oxford: Oxford Scientific Publications, Clarendon Press.

Khomyakov, A. P. & Sørensen, H. (2001). Zoning in steenstrupine-(Ce) from the Ilímaussaq alkaline complex, South Greenland: a review and discussion. *Geology of Greenland Survey Bulletin* **190**, 109–118.

Krumrei, T. V., Pernicka, E., Kaliwoda, M. & Markl, G. (2007). Volatiles in a peralkaline system: abiogenic hydrocarbons and F-Cl-Br systematics in the naujaite of the Ilímaussaq intrusion, South Greenland. *Lithos* **95**, 298–314.

Krumrei, T. V., Villa, I. M., Marks, M. A. W. & Markl, G. (2006). A $^{40}Ar/^{39}Ar$ and U/Pb isotopic study of the Ilímaussaq complex, South Greenland: implications for the ^{40}K decay constant and for the duration of magmatic activity in a peralkaline complex. *Chemical Geology* **227**, 258–273.

Langmuir, C. H. (1989). Geochemical consequences of in situ crystallization. *Nature* **340**, 199–205.

Larsen, L. M. (1977). Aenigmatites from the Ilímaussaq intrusion, South Greenland: chemistry and petrological implications. *Lithos* **10**, 257–270.

Larsen, L. M. & Sørensen, H. (1987). The Ilímaussaq intrusion-progressive crystallization and formation of layering in an agpaitic magma. In: Fitton, J.G. & Upton, B.G.J. (eds), *Alkaline Igneous Rocks. Geological Society of London, Special Publication* **30**, 473–488.

Lauder, W. R. (1964). Mat' formation and crystal settling in magma. *Nature* **202**, 1100–1101.

Lindhuber, M. J., Marks, M. A. W., Bons, P. D., Wenzel, T. & Markl, G. (2015). Crystal mat-formation as an igneous layering-forming process: textural and geochemical evidence from the 'lower layered' nepheline syenite sequence of the Ilímaussaq complex, South Greenland. *Lithos* **224–225**, 295–309.

Markl, G. & Baumgartner, L. (2002). pH changes in peralkaline late-magmatic fluids. *Contributions to Mineralogy and Petrology* **144**, 331–346.

Markl, G., Marks, M. A. W. & Frost, B. R. (2010). On the controls of oxygen fugacity in the generation and crystallization of peralkaline melts. *Journal of Petrology* **51**, 1831–1847.

Markl, G., Marks, M. A. W., Schwinn, G. & Sommer, H. (2001). Phase equilibrium constraints on intensive crystallization parameters of the Ilímaussaq Complex, South Greenland. *Journal of Petrology* **42**, 2231–2258.

Marks, M. A. W. & Markl, G. (2015). The Ilímaussaq Alkaline Complex, South Greenland. In: Charlier, B., Namur, O., Latypov, R. & Tegner, C. (eds) *Layered Intrusions*. Dordrecht: Springer, pp. 649–691.

Marks, M. A. W. & Markl, G. (2017). A global review on agpaitic rocks. *Earth-Science Reviews* **173**, 229–258.

Marks, M. A. W., Hettmann, K., Schilling, J., Frost, B. R. & Markl, G. (2011). The mineralogical diversity of alkaline igneous rocks: critical factors for the transition from miaskitic to agpaitic phase assemblages. *Journal of Petrology* **52**, 439–455.

Marks, M., Vennemann, T., Siebel, W. & Markl, G. (2004). Nd-, O-, and H-isotopic evidence for complex, closed-system fluid evolution of the peralkaline Ilímaussaq intrusion, South Greenland. *Geochimica et Cosmochimica Acta* **68**, 3379–3395.

Marsh, B. D. (1995). Solidification fronts and magmatic evolution. *Mineralogical Magazine* **60**, 5–40.

McBirney, A. R. & Noyes, R. M. (1979). Crystallization and layering of the Skaergaard intrusion. *Journal of Petrology* **20**, 487–554.

Müller-Lorch, D., Marks, M. A. & Markl, G. (2007). Na and K distribution in agpaitic pegmatites. *Lithos* **95**, 315–330.

Namur, O., Abily, B., Boudreau, A., Blanchette, F., Bush, J. W. M., Ceuleneer, G., Charlier, B., Donaldson, C. H., Higgins, M. D., Morata, D., Nielsen, T. F. D., O'Driscoll, B., Pang, K. N., Peacock, T., Spandler, C., Toramaru, A. & Veksler, I. (2015). Igneous layering in basaltic magma chambers. In: Charlier, B., Namur, O., Latypov, R. & Tegner, C. (eds) *Layered Intrusions*. Dordrecht: Springer, pp. 75–152.

Nielsen, T. F. D. & Bernstein, S. (2009). Chemical stratigraphy of the Triple Group and mineralization of the Skærgaard intrusion: insight in the crystallisation process. AGU Fall Meeting 2009, Abstract ID V21A-1956.

Nielsen, T. F. D., Andersen, J. C. Ø., Holness, M. B., Keiding, J. K., Rudashevsky, N. S., Rudashevsky, V. N., Salmonsen, L. P., Tegner, C. & Veksler, I. V. (2015). The Skaergaard PGE and gold deposit: the result of in situ fractionation, sulphide saturation, and magma chamber-scale precious metal redistribution by immiscible Fe-rich melt. *Journal of Petrology* **56**, 1643–1676.

Palme, H. & O'Neill, H. S. C. (2003). Cosmochemical estimates of mantle composition. *Treatise on Geochemistry* **2**, 1–38.

Paton, C., Hellstrom, J., Paul, B., Woodhead, J. & Hergt, J. (2011). Iolite: freeware for the visualisation and processing of mass spectrometric data. *Journal of Analytical Atomic Spectrometry* **26**, 2508–2518.

Parsons, I. (ed.) (1987). *Origins of Igneous Layering*. Dordrecht: D. Reidel.

Petersen, O. V., Johnsen, O., Gault, R. A., Niedermayr, G. & Grice, J. D. (2004). Taseqite, a new member of the eudialyte group from the Ilímaussaq alkaline complex, South Greenland. *Neues Jahrbuch für Mineralogie Monatshefte* **2004**, 83–96.

Pfaff, K., Wenzel, T., Schilling, J., Marks, M. A. W. & Markl, G. (2010). A fast and easy-to-use approach to cation site assignment for eudialyte group minerals. *Neues Jahrbuch für Mineralogie Abhandlungen* **187**, 69–81.

Pfaff, K., Krumrei, T. V., Marks, M. A. W., Wenzel, T., Rudolf, T. & Markl, G. (2008). Chemical and physical evolution of the 'lower layered series' from the nepheline syenitic Ilímaussaq intrusion, South Greenland: Implications for the origin of magmatic layering in peralkaline felsic liquids. *Lithos* **106**, 280–296.

Ratschbacher, B. C., Marks, M. A. W., Bons, P. D., Wenzel, T. & Markl, G. (2015). Emplacement and geochemical evolution of highly evolved syenites investigated by a combined structural and geochemical field study: the lujavrites of the Ilímaussaq Complex, SW Greenland. *Lithos* **231**, 62–76.

Reeder, R. J. & Rakovan, J. (1999). Surface structural controls on trace element incorporation during crystal growth. In: Jamtveit B & Meakin P. (eds) *Growth, Dissolution and Pattern-Formation in Geosystems*. Norwell, MA: Kluwer Academic Publishers, pp. 143–162.

Rønsbo, J. G., Sørensen, H., Roda-Robles, E., Fontan, F. & Monchoux, P. (2014). Rinkite–nacareniobsite-(Ce) solid solution series and hainite from the Ilímaussaq alkaline complex: occurrence and compositional variation. *Bulletin of the Geological Society Denmark* **62**, 1–15.

Schilling, J., Wu, F. Y., McCammon, C., Wenzel, T., Marks, M. A. W., Pfaff, K., Jacob, D. E. & Markl, G. (2011). The compositional variability of eudialyte-group minerals. *Mineralogical Magazine* **75**, 87–115.

Schønwandt, H. K., Barnes, G. B. & Ulrich, T. (2016). A description of the world-class rare earth element deposit, Tanbreez, South Greenland. In: Borges de Lima, I & Filho, W.L. (eds) *Rare Earths Industry*. Boston: Elsevier, pp. 73–85.

Sørensen, H. (1969). Rhythmic igneous layering in peralkaline intrusions: an essay review on Ilímaussaq (Greenland) and Lovozero (Kola, USSR). *Lithos* **2**, 261–283.

Sørensen, H. (1992). Agpaitic nepheline syenites: a potential source of rare elements. *Applied Geochemistry* **7**, 417–427.

Sørensen, H. (1997). The agpaitic rocks—an overview. *Mineralogical Magazine* **61**, 485–498.

Sørensen, H. & Larsen, L. M. (1987). Layering in the Ilímaussaq alkaline intrusion, South Greenland. In: Parsons, I. (ed.) *Origins of Igneous Layering*. Dordrecht: D. Reidel, pp. 1–28.

Sørensen, H. & Larsen, L. M. (2001). The hyper-agpaitic stage in the evolution of the Ilímaussaq alkaline complex, South Greenland. *Geological Survey of Denmark and Greenland Bulletin* **190**, 83–94.

Sørensen, H., Bailey, J. C. & Rose-Hansen, J. (2011). The emplacement and crystallization of the U-Th-REE rich agpaitic and hyperagpaitic lujavrites at Kvanefjeld, Ilímaussaq alkaline complex, South Greenland. *Bulletin of the Geological Society of Denmark* **59**, 69–92.

Sørensen, H., Bohse, H. & Bailey, J. C. (2006a). The origin and mode of emplacement of lujavrites in the Ilímaussaq alkaline complex, South Greenland. *Lithos* **91**, 286–300.

Sørensen, H., Andersen, T., Emeleus, C. H., Secher, K., Upton, B. G. J. & Weidick, A. (2006b). *Geological Guide to South Greenland*. Copenhagen: Geological Survey of Denmark and Greenland.

Steenfelt, A. & Bohse, H. (1975). Variations in the content of uranium in eudialyte from the differentiated alkaline Ilímaussaq intrusion, South Greenland. *Lithos* **8**, 39–45.

Upton, B., Emeleus, C., Heaman, L., Goodenough, K. & Finch, A. (2003). Magmatism of the mid-Proterozoic Gardar Province, South Greenland: chronology, petrogenesis and geological setting. *Lithos* **68**, 43–65.

Upton, B. G. J. (2013). Tectono-magmatic evolution of the younger Gardar southern rift, South Greenland. *Geological Survey of Denmark and Greenland Bulletin* **29**, 1–128.

Ussing, N. V. (1912). Geology of the country around Julianehaab, Greenland. *Meddelelser om Grønland* **38**, 426.

Wager, L. R. & Brown, G. M. (1967). *Layered Igneous Rocks*. Edinburgh: Oliver & Boyd**, p. 588**.

Wager, L. R., Brown, G. M. & Wadsworth, W. J. (1960). Types of igneous cumulates. *Journal of Petrology* **1**, 73–85.